Closed-loop optogenetic control of normal and pathological network dynamics

Boubker Zaaimi
Newcastle University
Mark Turnbull
Newcastle University
Anupam Hazra
Newcastle University
Yujiang Wang
Newcastle University
Carolina Gandara de Souza
Newcastle University
Enrique Escobedo-Cousin
Newcastle University
Ahmad Idil
University College London
Richard Bailey
Newcastle University https://orcid.org/0000-0001-7367-766X
Sabrina Tardio
Newcastle University
Aaliyah Patel
Newcastle University
Nikhil Ponon
Newcastle University
Frances Hutchings
Newcastle University
Marcus Kaiser
Newcastle University
Mark Cunningham
Trinity College Dublin
Gavin Clowry
Newcastle University
Fiona LeBeau
Newcastle University
Timothy Constandinou

Imperial College London https://orcid.org/0000-0001-9778-1162
Stuart Baker
Newcastle University
Nick Donaldson
University College London
Patrick Degenaar
Newcastle University
Anthony O'Neill
Newcastle University
Andrew Trevelyan
Newcastle University
Andrew Jackson (andrew.jackson@newcastle.ac.uk)
Newcastle University

Article

Keywords: Closed-loop optogenetic control, network dynamics, excitatory opsins (CLOSe), electrical neurostimulation

Posted Date: October 6th, 2020

DOI: https://doi.org/10.21203/rs.3.rs-78230/v1

Version of Record: A version of this preprint was published at Nature Biomedical Engineering on October 20th, 2022. See the published version at https://doi.org/10.1038/s41551-022-00945-8.

Closed-loop optogenetic control of normal and pathological network dynamics

Authors: B Zaaimi[1,2], M Turnbull[1], A Hazra[1], Y Wang[3], CG de Souza[1], E Escobedo-Cousin[4], AS Idil[5], R Bailey[4], S Tardio[4], A Patel[4], N Ponon[4], F Hutchings[3], M Kaiser[3], MO Cunningham[6], GJ Clowry[1], FE LeBeau[1], TG Constandinou[7], SN Baker[1], N Donaldson[5], P Degenaar[4], A O'Neill[4], AJ Trevelyan[1], A Jackson[1,8]

1. *Biosciences Institute, Newcastle University, Newcastle NE2 4HH, UK*
2. *Current address: School of Life and Health Sciences, Aston University, Birmingham B4 7ET, UK*
3. *School of Computing, Newcastle University, Newcastle NE4 5TG, UK*
4. *School of Engineering, Newcastle University, Newcastle NE1 7RU, UK*
5. *Department of Medical Physics and Biomedical Engineering, UCL, London WC1E 6BT, UK*
6. *School of Medicine, Trinity College Dublin, Dublin 2, Ireland*
7. *Department of Electrical and Electronic Engineering, Imperial College, London SW7 2AZ, UK*
8. *To whom correspondence should be addressed (andrew.jackson@ncl.ac.uk)*

Electrical neurostimulation is effective in treating neurological disorders, but associated recording artefacts generally limit applications to 'open-loop' stimuli. Since light does not prevent concurrent electrical recordings, optogenetics enables real-time, continuous 'closed-loop' control of brain activity. Here we show that closed-loop optogenetic stimulation with excitatory opsins (CLOSe) affords precise manipulation of neural dynamics, both *in vitro*, in brain slices from transgenic mice, and *in vivo,* with anesthetised monkeys. We demonstrate the generation of oscillations in quiescent tissue, enhancement or suppression of endogenous patterns in active tissue, and modulation of seizure-like bursts elicited by 4-aminopyridine. New network properties, emergent under CLOSe, depended on the phase-shift imposed between neural activity and optical stimulation, and could be modelled with a nonlinear dynamical system. In particular, CLOSe could stabilise or destabilise limit cycles associated with seizure oscillations, evident from systematic changes in the variability and entropy of seizure trajectories that correlated with their altered duration and intensity. Furthermore, CLOSe was achieved using intracortical optrodes incorporating light-emitting diodes, paving the way for translation of closed-loop optogenetics towards therapeutic applications in humans.

Many neurological conditions lead to altered network dynamics, characterised by abnormally low or high levels of oscillatory synchrony within, and between, brain areas (Uhlhaas and Singer, 2006). Neuromodulation therapies such as Deep Brain Stimulation (DBS) typically deliver 'open-loop' trains of electrical stimulation in an attempt to disrupt pathological patterns and maintain brain activity within a range of functional states. However, from a control theory perspective, open-loop methods are generally inferior to closed-loop control that incorporates feedback based on the real-time state of the system (Shanechi, 2019). Thus, neuromodulation therapies may be more effective if controlled by ongoing electrophysiological measurements (Bouthour et al., 2019, Cagnan et al., 2019), for example to enhance beneficial oscillations or to destabilise pathological brain states such as epileptic seizures. Unfortunately, many potential applications of closed-loop neurostimulation are hampered by large artefacts associated with electrical stimulation, particularly when monitoring and modulating the same local population of neurons. This often limits control policies to simple decisions to turn on or off otherwise continuous trains of stimuli (Little et al., 2013, Skarpaas et al., 2019).

Since the light stimuli used for optogenetics can be delivered without preventing concurrent electrical recording, it can be continuously modulated in real-time by brain signals to allow true closed-loop interaction with local networks. Despite considerable theoretical motivation (Grosenick et al., 2015), experimental demonstrations of closed-loop optogenetic stimulation have thus far been limited to *in*

vitro preparations (Nicholson et al., 2018) and *in vivo* experiments on normal brain rhythms in rodents (Sohal et al., 2009, Siegle and Wilson, 2014, Stark et al., 2014). Here we aim to advance this technique towards therapeutic applications in humans, by demonstrating the feasibility of closed-loop manipulation of network dynamics in non-human primates and examining its effect on pathological seizure-like activity. In addition, we compare optical stimulation delivered via an external light source with an implantable optrode incorporating encapsulated light-emitting diodes (LEDs). While optogenetics allows specific cell types to be targeted with a range of different opsins, we focus here on closed-loop optogenetic stimulation with excitatory opsins (CLOSe), using efficient ion channel opsins without the need to restrict expression to specific neuronal subtypes. We hypothesized that by altering the timing of stimulation relative to ongoing activity, we could exert differential effects on the local networks, thus adding a new temporal dimension to the control of neural dynamics that can be achieved with optogenetics.

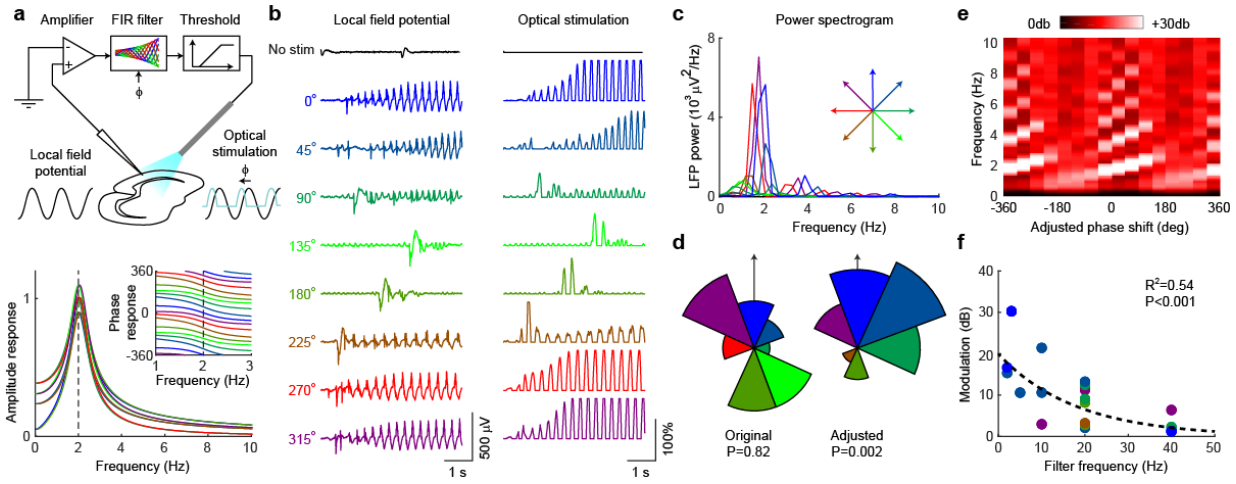

Figure 1 - CLOSe drives oscillations in quiescent mouse brain slices. **a** *Top:* Schematic of experimental setup. LFP, recorded from an Emx1-ChR2 mouse, brain slice was filtered and used to control optical stimulation in real-time. *Bottom:* Amplitude response of filter. Inset shows phase response across the passband. **b** Example LFP and stimulation traces under no stimulation (black) and CLOSe with different phase-shifts (relative to LFP, 2 Hz filter frequency). **c** LFP power spectra for different phase-shifts. **d** *Left:* Phase-shifts (relative to LFP) associated with maximal oscillation in 21 sessions. *Right:* Adjusted phase-shifts (relative to high gamma activity; see Supp. Fig. 1). P values from Rayleigh test for circular non-uniformity. **e** LFP power at different frequencies for different adjusted phase-shifts (2 Hz filter). Phase-shift is unwrapped and plotted over two cycles. **f** Phase-dependent modulation of LFP power for different filter frequencies. Colour indicates adjusted phase-shift associated with maximal oscillation. Dashed line shows log-linear fit to data.

Closed-loop optogenetic stimulation drives oscillations in quiescent brain slices

We first investigated CLOSe in quiescent brain slices taken from transgenic mice, expressing channelrhodopsin selectively in excitatory pyramidal cells (Emx1-ChR2). The local field potential (LFP), recorded with an extracellular electrode, was passed through a finite impulse response (FIR) filter using a kernel which band-passed and phase-shifted the signal (Fig. 1a). The output of the filter was half-wave rectified (above a threshold set to reject background noise) and controlled in real-time the intensity of optical stimulation delivered through a light fibre. Within each experimental session we delivered CLOSe epochs with different phase-shifts (0, 45°, …, 315°) in pseudorandomised order, interspersed by control epochs with no stimulation. Across different sessions, we tested filters with central frequencies between 2-40 Hz.

Application of CLOSe with some phase-shifts produced no stable oscillation, while others created a positive feedback loop which drove strong oscillations at frequencies within the filter pass-band (Fig. 1b,c). Qualitatively similar effects were obtained in 21 sessions with different slices, but we observed considerable variation in the phase-shift associated with maximal LFP oscillations (Supp. Fig. 1a, Fig. 1d *left*; circular mean=-27°, Raleigh test for circular non-uniformity P=0.82). We speculated that this was due to variation in the relationship between LFPs and underlying neural activity, which is known to vary through the cortex (Hall et al., 2014). Therefore, we used the envelope of high-gamma (>100 Hz) LFP activity as a surrogate of neural firing, and calculated the zero-lag phase of its cross-correlation with the LFP in each session (Supp. Fig. 1b). Off-line, we added this correction to the phase-shift applied by the filter in order to replot our data against an adjusted phase-shift that represented the overall phase-advance of optical stimulation relative to putative neural activity (Supp. Fig. 1c). Following this adjustment, the phase-shift associated with maximal positive-feedback LFP oscillations was consistently around 0-90° relative to the high gamma envelope (Fig. 1d, *right*, circular mean=38°, Rayleigh test for circular non-uniformity P=0.002), while phase-shifts around 180-270° were associated with minimal oscillation. We refer to these conditions as CLOSe^{+} and CLOSe^{-} respectively. CLOSe^{+} drove oscillations around the centre-frequency of the filter as well as higher harmonics, and these frequencies increased systematically with increasing phase-shift, as shown by the diagonal stripes in Fig. 1e (note that phase-shift is unwrapped and plotted over two cycles). Conceptually, this behaviour can be understood by equating a phase-advance in the feedback signal with a reduction of the feedback loop delay. As this delay is reduced, the frequencies associated with positive feedback instabilities increase. By altering the central filter frequency, we were able to tune these resonant frequencies (Supp. Fig. 1a) and drive oscillations up to 40 Hz, although the LFP power modulation was significantly reduced at higher frequencies (Fig. 1f).

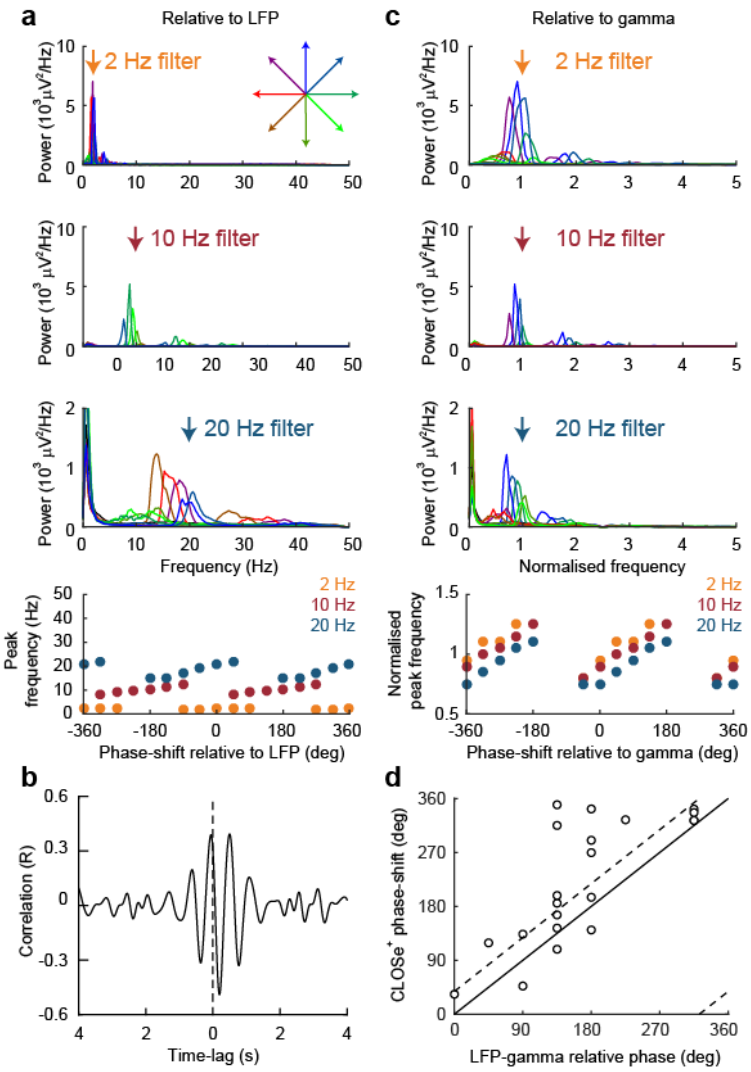

Supplemental Figure 1 – Realigning phase-shifts to high gamma envelope. a LFP spectra from three different Emx1-ChR2 mouse brain slice sessions. Bottom plot shows that the phase-shifts and frequencies of driven oscillations varied across sessions. **b** Cross-correlation between the LFP and high gamma envelope was used to infer the phase relationship between LFP and underlying neural activity. **c** LFP spectra replotted after adjusting phase-shift relative to high gamma envelope. In addition, the frequency axis has been normalised by the filter frequency. As a result, the frequencies of oscillations driven by different phase-shifts are more closely aligned. **d** Phase-shifts (relative to LFP) that drove maximal oscillation plotted against relative phase between LFP and high gamma envelope. Solid line indicates stimulation in phase with high gamma. Maximal modulation was typically obtained for phase-shifts advanced by 0-90° relative to this (circular mean 38°, *dashed line*).

CLOSe can boost or suppress endogenous in vivo activity in non-human primates

Next, we examined the effect of CLOSe on endogenous *in vivo* brain activity in two non-human primates (NHPs). Excitatory opsins were expressed under the neuron-specific human synapsin promoter (hSyn) using viral vectors [either AAV8-hSyn-Chronos-GFP or Lenti-hSyn-eYFP-2A-ChR2(H134R); Supp. Table 1] injected into the primary motor cortex, 7-19 weeks prior to recording sessions under terminal anaesthesia. Post-mortem histology confirmed widespread expression of associated fluorescent tags in both animals (Supp. Fig. 2a). LFPs and single-units were recorded with multi-contact electrodes. Open-loop stimulation (200 or 500 ms pulses at 1 Hz) and CLOSe (driven by different phase-shifts applied to one LFP from the array) was delivered through an optic ferrule inserted into the cortex. Figure 2a (*top*) shows example open-loop stimulation using ChR2. Large LFP deflections were observed in response to light pulses, associated with bursts of neural firing (Fig. 2b). Note that, unlike our EMX-ChR2 mice, the promoter used in the NHPs was not specific to excitatory neurons and, consistent with this, we occasionally observed suppression of firing in some neurons (Supp. Fig. 2b). Importantly, the polarity of field responses varied with depth, as expected for a physiological response rather than photoelectric artefact (Fig. 2b; *left*).

CLOSe^{+} again drove strong oscillatory responses in field potentials and neural firing (Fig. 2a; *middle*), revealed by cycle-triggered LFP averages (Fig. 2b). Note that the depth profile of the driven oscillations resembled that of endogenous activity observed during control epochs with no stimulation, suggesting that CLOSe^{+} drove naturalistic patterns of network activity (Supp. Fig. 3). Despite using an excitatory opsin, CLOSe was also capable of suppressing oscillations below levels seen with no stimulation. This can be seen in the cycle-triggered LFP averages for different phase-shifts (Fig. 2c) as well as in the LFP power spectra (Fig. 2d). Figure 2e shows oscillatory power at each frequency for each phase condition, normalised by the corresponding power spectrum for *no-stimulation* epochs. Regions of red reflect CLOSe^{+} driving positive feedback oscillations, while interspersed regions of blue show CLOSe^{-} phase-shifts that suppressed background activity. No such modulation was observed in control experiments using a frequency of light that was outside the opsin absorption spectrum delivered through the same optic ferrule (Fig. 2f), demonstrating our results were mediated by optogenetic stimulation rather than non-specific effects such as photoelectric artefacts or tissue heating.

We additionally tested CLOSe delivered via an implanted optrode incorporating LED light sources placed inside the brain. Significant modulation of field potential power could also be obtained using a single LED (Fig. 2g and Supp. Fig. 4a), albeit with a weaker magnitude, consistent with the LED producing about half the light power of our commercial fibre-coupled system (Supp. Fig. 4b). Figure 2h shows modulation of power around the closed-loop filter frequency, with a statistically significant effect of the eight phase conditions for illumination with blue light via the ferrule (circular-linear correlation, n=57 stimulation epochs, R=0.90, P=1×10^{-10}) and LED (n=60, R=0.86, P=2×10^{-10}) but not for control yellow light (n=58, R=0.13, P=0.6). We observed statistically significant (circular-linear correlation, P<0.05) phase-dependent power modulation in experiments made in three hemispheres from two animals (Figure 2i), using both opsins (Supp. Table 1). Once again, we could tune the frequencies of enhancement and suppression by altering the filter frequencies. We quantified modulation from both the maximum/minimum modulation of LFP power for any single phase-shift (*raw data*, Fig. 2j *top*) and from a sinusoidal fit through all phase-shifts (*sine fit*, Fig. 2j *bottom*). As with the brain slice experiments, modulation became progressively weaker for higher closed-loop filter frequencies, with statistically significant phase-dependence at 40 Hz observed in only two of the three datasets.

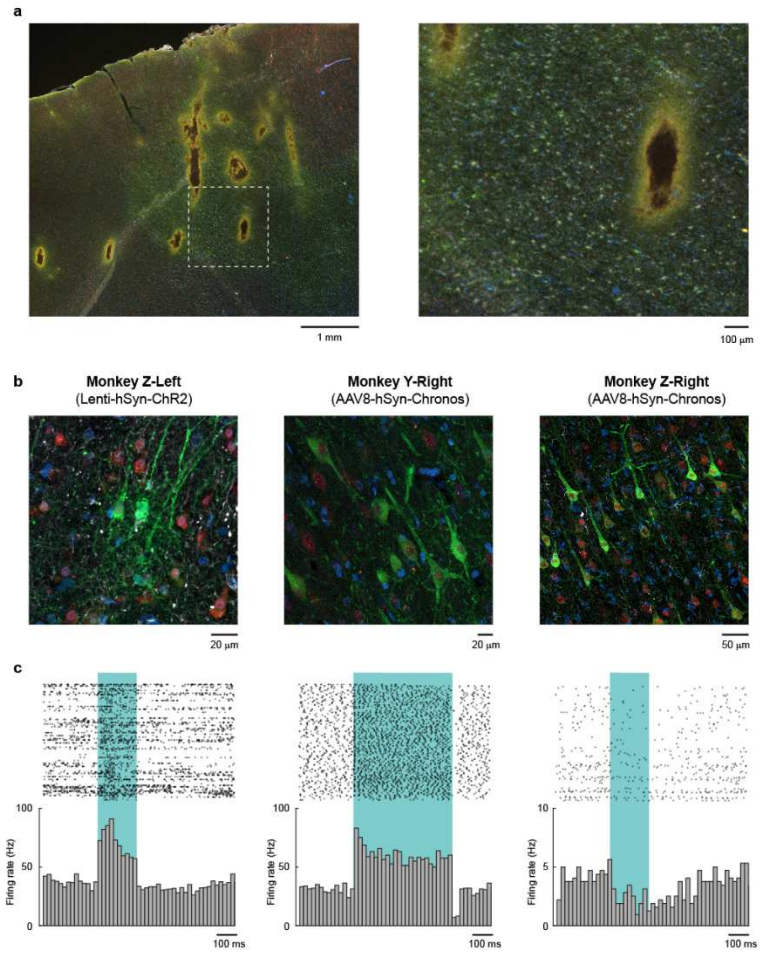

Supplemental Figure 2 – Viral expression of opsins in NHP. a *Left:* Post-mortem images of Monkey Z (left hemisphere). The four holes linearly spaced 1.25 mm apart are from the prongs of the LED fork. Other tracks likely reflect recording electrodes, light ferrule and/or 4-AP injections. *Right:* Zoomed image shows staining for fluorescent marker (green) in cells in this area. **b** Confocal imaging in the three hemispheres from two animals demonstrating expression of fluorescent marker (green) in neurons including pyramidal neurons, co-localised with NeuN neuronal marker (red). Also overlain is Hoechst nuclear stain (blue) and GFAP astrocytic marker (white). **c** Example spike raster plots and peri-stimulus histograms showing optogenetic responses in neurons recorded from the three hemispheres. Two cells show strong excitatory responses to blue light stimulation (shaded region), while one cell is inhibited, possibly mediated by inhibitory interneurons due to the non-selective promotor.

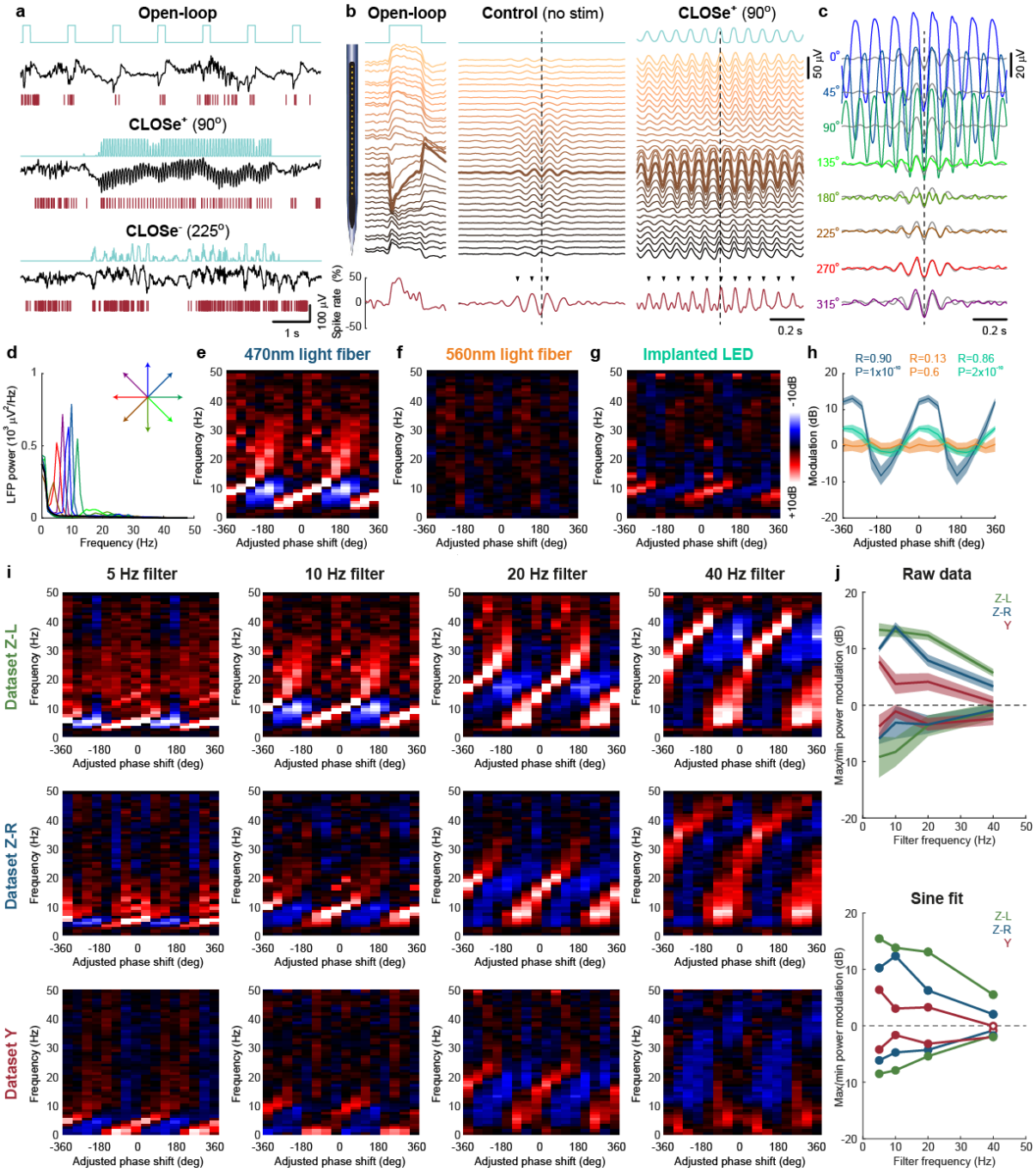

Figure 2 - CLOSe modulates endogenous activity *in vivo* in non-human primates. a Example LFP and spike activity during open-loop stimulation and 5 s CLOSe epochs with two different phase-shifts (10 Hz filter) recorded from monkey motor cortex injected with Lenti-hSyn-eYFP-2A-ChR2(H134R). **b** *Left:* Stimulus-triggered average LFP and neural response to open-loop stimulation. Stacked traces indicate LFP recorded from different electrodes on the linear array (3 mm total). The thick line indicates LFP used for CLOSe. Multiple phase reversals are evident in the response. *Right:* LFP cycle-triggered averages (aligned to troughs in the CLOSe LFP, dashed line) during no stimulation and CLOSe^{+}. Tick marks indicate significant increased spike rate (average of 21 cells) compared to shuffled surrogates. Note that the LFP phase reversal observed in the endogenous activity matches that driven by optical stimulation. **c** Cycle-triggered averages for all CLOSe phase-shifts. Note that CLOSe^{-} reduced the amplitude of LFP

cycles relative to no stimulation (grey traces). **d** LFP power spectra for epochs of CLOSe with different phase-shifts. **e** Relative power modulation for different CLOSe phase-shifts, showing frequencies with increased (red) and reduced (blue) activity relative to no stimulation. **f** No modulation was observed when stimulating with a frequency of light outside the opsin absorption range. **g** LFP modulation driven by an implanted LED. **h** LFP modulation (between 0.8-1.2x the filter frequency) for the three datasets. R and P values from circular-linear correlation over stimulation epochs. **i** LFP modulation for different filter frequencies replicated in three datasets (Z-L: Lenti-hSyn-eYFP-2A-ChR2(H134R); Z-R and Y: AAV8-hSyn-Chronos-GFP). **j** Maximum/minimum power modulation (between 0.8-1.2x the filter frequency) for different filter frequencies. *Top:* maximum/minimum value for any phase-shift. Shading indicates s.e.m. over stimulation epochs. *Bottom:* maximum/minimum values of sinusoidal fit to data. Filled circles indicate significant phase-dependent modulation (circular-linear correlation over stimulus epochs, $P<0.05$).

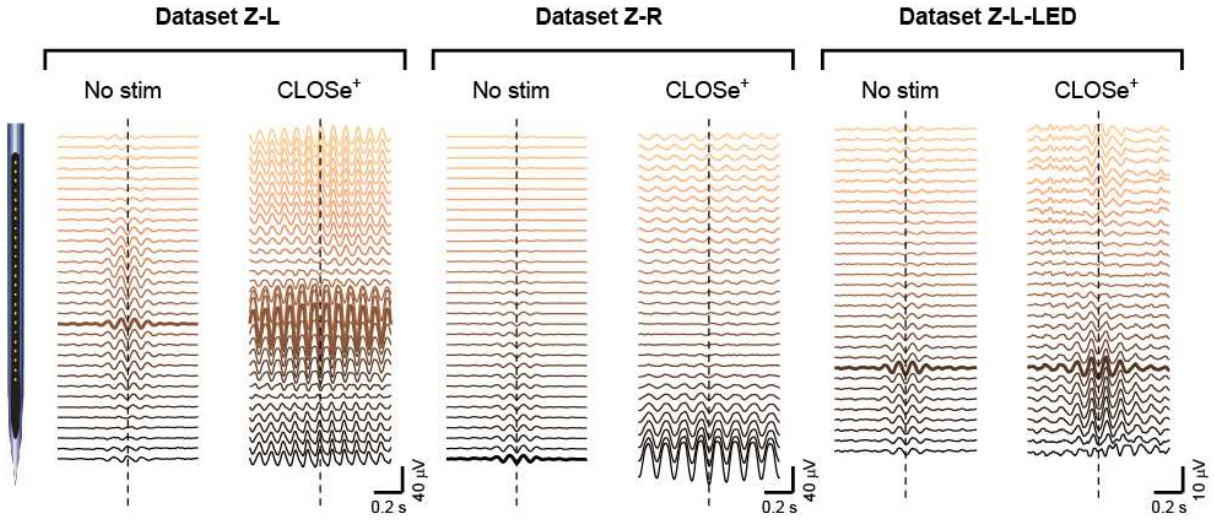

Supplemental Figure 3 – Depth profile of endogenous and evoked oscillations. Cycle-triggered average (aligned to troughs in the CLOSe LFP, dashed line) traces from different electrodes in the linear array (3 mm total) during no stimulation and CLOSe$^+$. The thick line indicates LFP used for CLOSe. Note the similar depth profile of endogenous and evoked oscillations, suggesting CLOSe$^+$ drove naturalistic patterns of network activity. Datasets Z-L: Lenti-hSyn-eYFP-2A-ChR2(H134R); Z-L and Y: AAV8-hSyn-Chronos-GFP; Z-L-LED driven by implanted LED instead of light fibre.

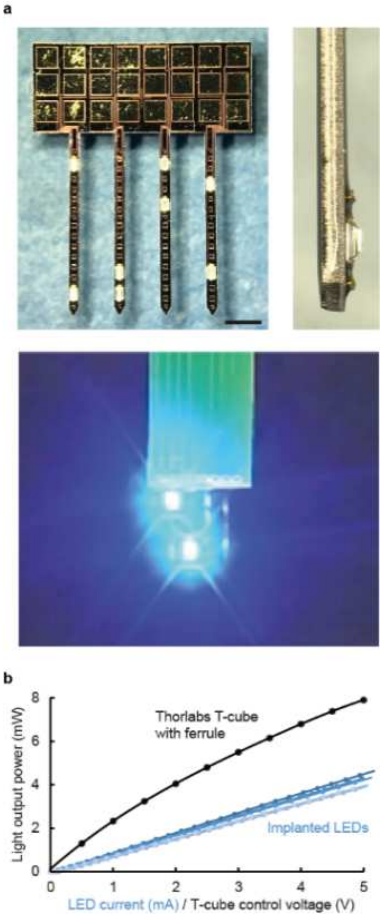

Supplemental Figure 4 – Implantable LED array used in NHP experiments. a Images of the silicon fork optrode comprising four shanks with 2 CREE DA2432 LEDs per shank encapsulated with silicone elastomer (NuSil MED-6015). Scale bar: 1 mm. **b** Measured light power output of each LED for different supply currents (blue). Also shown is the light power output for the commercial light source used for the other datasets. The horizontal axis encompasses the full range of stimulation intensities in both cases. Note that the datasets analysed here used a single LED to activate the tissue.

CLOSe can modulate pharmacologically-induced epileptiform activity in vitro

Having demonstrated phase-shift-dependent enhancement and suppression of endogenous oscillations, we next examined whether CLOSe could influence pharmacologically-induced pathological states resembling seizures. In our *in vitro* brain slice model, bath application of 4-aminopyridine (4-AP) generated sporadic seizure-like events consisting of multiple brief bursts of oscillatory discharge around 15-20 Hz. An example of this activity is shown in Figure 3a. Applying CLOSe with a 20 Hz filter frequency in this session could shorten the duration of individual bursts depending on phase-shift (Fig. 3b, *left*). Figure 3b (*right*) shows a logarithmic plot of the modulation of burst durations under different CLOSe phase-shifts relative to *no-stimulation* epochs. Across this whole session, the burst duration was doubled under $CLOSe^{+}$ (0° phase-shift, mean ± s.e.m. $\log_2$-ratio burst duration = 1.00 ± 0.18) and decreased by about a quarter under $CLOSe^{-}$ (225° phase-shift, $\log_2$-ratio burst duration = -0.44 ± 0.15). Circular-linear correlation across the eight phase-shift conditions confirmed that modulation of burst duration depended significantly on closed-loop phase-shift (n=221

seizure bursts, R=0.62, P=1x10^{-16}). Modulation was also evident as phase-dependent enhancement and suppression of LFP power spectra during seizure-like events (Fig. 3c). Averaged across our dataset of 10 sessions, the relative duration of seizure bursts was modulated between a max/min $\log_2$-ratio of 0.49 ± 0.13 to -0.48 ± 0.11 (equivalent to 1.4x increase and 0.7x decrease respectively; Fig. 3d), and depended significantly on closed-loop phase-shift in 8/10 individual sessions (circular-linear correlation, P<0.05). When all sessions were combined (after adjusting to high-gamma activity as before), the relative burst duration also depended significantly on CLOSe phase-shift (circular-linear correlation, n=10 sessions x 8 phase conditions, R=0.29, P=0.03), as did power modulations at seizure frequencies (Fig. 3e, n=80, R=0.39, P=0.002). Note however that our (high-gamma) phase-shift adjustment did not perfectly align the different sessions so the max/min modulation in the session-averaged plots was lower than that seen in individual sessions, and no single phase-shift produced statistically significant suppression in the combined dataset.

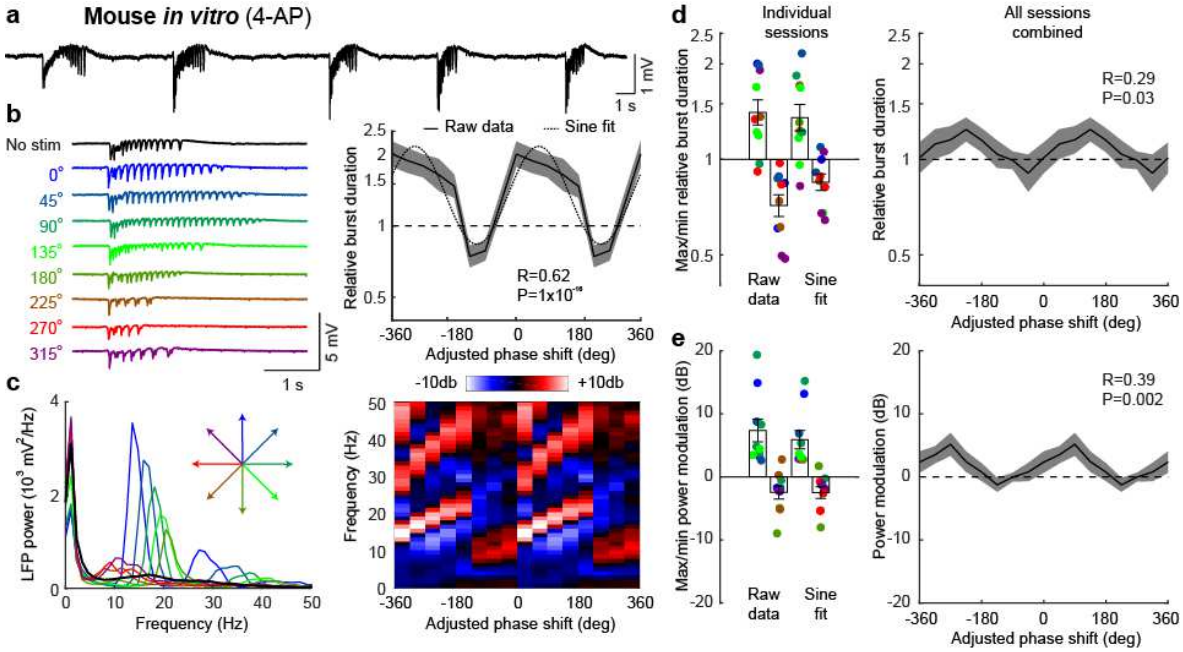

Figure 3 - CLOSe modulates 4AP-induced epileptiform activity in mouse brain slices. a Example seizure-like event comprising multiple bursts elicited by bath application of 4-AP to Emx-ChR2 mouse brain slices. **b** *Left:* Individual seizure bursts under CLOSe (20 Hz filter) with different phase-shifts showing phase-dependent prolongation and shortening of burst duration. *Right:* Average burst duration relative to no stimulation for different CLOSe phase-shifts. Shading indicates s.e.m. over bursts. R and P values from circular-linear correlation over bursts. Dashed line shows sinusoidal fit. **c** *Left:* LFP power spectra during seizure-like events under different CLOSe phase-shifts. *Right:* Modulation of LFP power relative to no stimulation. **d** *Left:* Max/min modulation of burst duration across 10 sessions for raw data and sinusoidal fit. Colour shows phase-shift associated with max/min for individual sessions. *Right:* Average modulation of burst duration averaged across sessions. **e** Same but for LFP power at seizure frequency. Error bars indicate s.e.m. over sessions. R and P values from circular linear correlation over datasets.

CLOSe can modulate pharmacologically-induced epileptiform activity in vivo

In the non-human primates *in vivo*, injection of 4-AP into the motor cortex reliably produced prolonged seizure events lasting around 20 s occurring at regular intervals (typically every minute for about an hour). Seizure events were characterised by an initial oscillation in the range 15-25 Hz followed by post-ictal discharges. Figure 4a shows two events from the right hemisphere of monkey Z (Chronos opsin); the first during a control period with no stimulation, and the second during delivery of CLOSe$^-$ with a phase-shift of 225° with a marked suppression of oscillatory discharge. Unlike the *in vitro* data, background activity and seizure variability precluded precise identification of the onset and offset of individual events. Therefore, to visualise the impact of CLOSe across the entire session, we instead computed the autocorrelation of the LFP amplitude envelope within the seizure band (10-30 Hz) over the whole duration of CLOSe and control epochs. The peaks in Fig. 4b with a width of approximately 20s reveal the broad temporal structure of seizures bursts, and the variation in their height and width indicates modulation by closed-loop stimulation. We quantified seizure magnitude by calculating the area under this curve (between ±20 s), although note that this single measure is influenced by the intensity, duration and interval between individual events. In addition, we calculated power spectra, across all epochs for each stimulation condition (Fig. 4c), which, when normalised by the *no-stimulation* spectra, again revealed a characteristic pattern of phase-dependent modulation (Fig. 4d). Similar results were obtained in two animals (Fig. 4e), as well as one session in which stimulation was delivered using the implanted LED (Fig. 4f). Across our dataset of 4 sessions, seizure magnitude was modulated by CLOSe between a $\log_2$ ratio of 1.11 ± 0.25 to -0.66 ± 0.13 (a 2.1x increase and 0.6x suppression respectively). When these data were combined, we observed a statistically significant effect of phase-shift on seizure magnitude (n=4 sessions x 8 phase conditions, R=0.70, P=0.0004; Fig. 4g) as well as corresponding modulation of LFP power at seizure frequencies (n=32, R=0.67, P=0.0007; Fig. 4h).

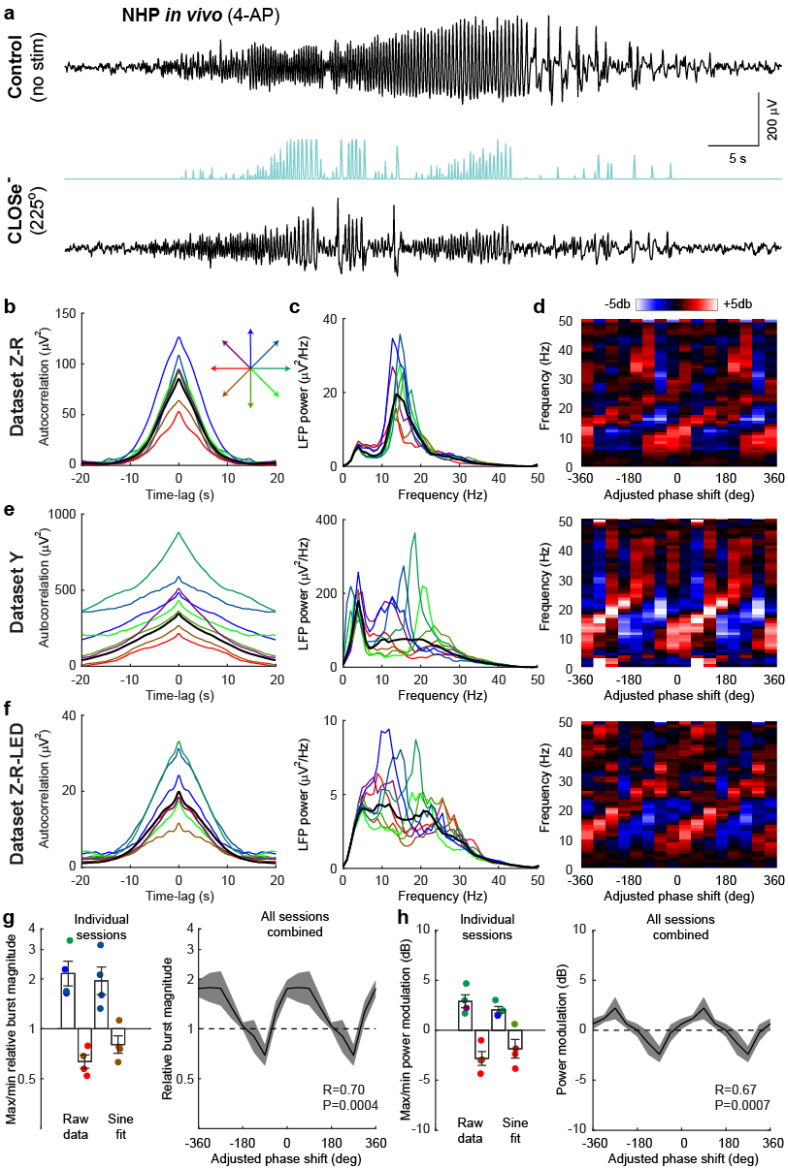

Figure 4 - CLOSe modulates 4AP-induced epileptiform activity *in vivo* in non-human primates. a *Top:* Example seizure-like event elicited by intracortical injection of 4-AP in monkey motor cortex. *Bottom:* Example seizure-like event under CLOSe⁻ (15 Hz filter frequency). **b** Autocorrelation of seizure-band LFP amplitude envelope reveals temporal structure of seizure burst under no stimulation (black). Coloured traces show modulation by CLOSe with different phase-shifts. **c** *Left:* LFP power spectra under different CLOSe phase-shifts. *Right:* Modulation of LFP power relative to no stimulation. **e** Same for replication in a second animal. **f** Same for replication using implanted LED to deliver light. **g** *Left:* Max/min modulation of burst magnitude (area under autocorrelation peak) across 4 datasets for raw data and sinusoidal fit. Colour shows phase-shift associated with max/min for individual datasets. *Right:* Average modulation of burst magnitude averaged across datasets. **h** Same but for LFP power at seizure frequency. Error bars indicate s.e.m. over datasets. R and P values from circular linear correlation over datasets.

CLOSe can stabilise or destabilise pathological network dynamics

Epileptic activity is usually thought to reflect an excess of excitatory activity in brain networks. Therefore, our observation that excitatory stimulation can reduce the duration and intensity of seizures is counterintuitive. To examine how CLOSe$^-$ was capable of attenuating seizure-like events, we simulated a simple Wilson-Cowan neural mass model that has previously been applied to epileptic activity (Wang et al., 2012, Wang et al., 2014). The model comprised two interconnected neural populations (excitatory and inhibitory) whose activity was represented in a two-dimensional phase space. The instantaneous state evolved through time according to nonlinear dynamics, which divided the phase space into two regimes (Fig. 5a). States initiated with low excitatory activity evolved towards a stable fixed point representing a quiescent network, while initial states with higher excitatory activity were attracted towards a limit cycle representing epileptiform oscillations. Connection weights were chosen to produce an oscillation frequency similar to the experimental data and Gaussian noise input was added to both populations, allowing probabilistic transitions between quiescent and seizure regions. CLOSe was modelled as an additional excitatory input to the excitatory population, dependent on a phase-shifted LFP signal reflecting a high-pass filtered combination of the activity of both populations.

Model simulations starting from the limit cycle under different closed-loop feedback conditions qualitatively captured many features of our experimental data (Fig. 5b, c.f. Fig. 3b,c), including phase-shift-dependent lengthening or shortening of seizure durations, and associated modulation of spectral power. To understand this better, we examined the behaviour of the seizure limit cycle under different CLOSe conditions (Fig. 5c and Supp. Movie 1). In the absence of input noise, excitatory stimulation alone never halted the seizure, but as the phase-shift advanced from CLOSe$^+$ to CLOSe$^-$, the limit cycle underwent period doubling and became increasingly complex, fluctuating between small and large cycles in the phase space. Since the larger cycles came close to the boundary of the quiescent regime, there was a higher probability that the added noise input could push the network across into the attractor basin of the stable fixed point (Fig. 5d). In other words, the altered duration of seizure bursts relative to the *no-stimulation* condition in our model could be explained by the increased stability (in the presence of input noise) of the limit cycle under CLOSe$^+$, and its increased sensitivity to noise perturbations under CLOSe$^-$.

To seek evidence for this phenomenon in our experimental data, we used delay embedding to reconstruct the dynamics of simulated and actual LFP data. Figure 5e,f and Supp. Fig. 5 shows 2- and 3-D projections of delay-embedded trajectories for the *in silico* simulation and for an example *in vitro* session. There are striking qualitative similarities between the model and experimental data; some phases of closed-loop stimulation are associated with simple, planar cycles whilst other phases generate complex and twisted trajectories. We quantified trajectories using two metrics: (i) the Coefficient of Variation (CV) of the radius, and (ii) approximate entropy (AppEn), which is an information theoretic measure of complexity that has previously been applied to seizure data (Zhou et al., 2012). For both simulated and experimental data, these metrics showed a phase-shift-dependent modulation, with lower/higher trajectory variability and entropy associated with CLOSe$^+$/CLOSe$^-$ respectively, relative to *no stimulation* (Fig. 4g). For both the *in vitro* (Fig. 4h) and *in vivo* datasets (Fig. 4i), trajectory CV and AppEn were inversely correlated with seizure duration and seizure severity ($P<0.05$ in all cases), providing evidence that the enhancement and suppression of epileptiform activity are associated with closed-loop feedback that respectively stabilises and destabilises the seizure cycle.

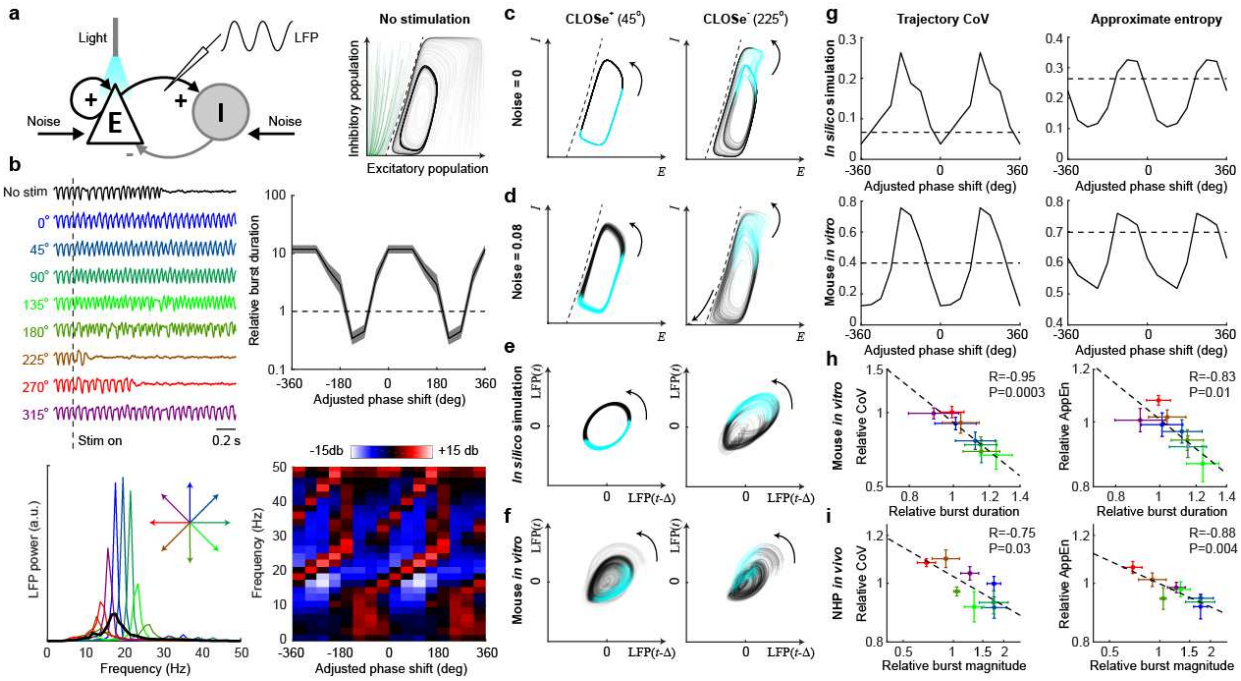

Figure 5 – *In silico* model suggests CLOSe can stabilise/destabilise seizure cycles. a *Left:* Schematic of *in silico* model comprising interconnected excitatory (E) and inhibitory (I) populations with white noise input. *Right:* Model trajectories evolving in the state-space. In the absence of noise, trajectories in green converge on a stable fixed point while trajectories in grey converge on a limit cycle. Dashed line indicates the separatrix between these regions. **b** *Top left:* Simulated seizure bursts under CLOSe with different phase-shifts. Simulations were initiated on the limit cycle prior to onset of CLOSe (dashed line), and used the same noise input. *Top right:* Modulation of burst duration relative to no stimulation for different CLOSe phase-shifts. Shading indicates s.e.m. over 20 iterations with different noise seeds. *Bottom:* Modulation of LFP power relative to no stimulation. **c** State-space trajectories under CLOSe^{+} and CLOSe^{-} in the absence of noise. Blue indicates when stimulation is delivered. Note that CLOSe^{-} increases the complexity of the trajectory. See Supp. Movie 1 for trajectories under all phase-shifts. **d** State-space trajectories in the presence of noise. The trajectory fluctuations under CLOSe^{-} are exacerbated, increasing the probability that noise takes the system into the point attractor basin. **e** Model dynamics reconstructed from delay-embedding of simulated LFP. Under CLOSe^{+} the LFP traces consistent cycles, while under CLOSe^{-} the trajectory is more complex and variable. **f** Delay-embedded trajectories for example *in vitro* session show a similar pattern. **g** Cycles were quantified with trajectory coefficient of variation (CoV, *left*) and approximate entropy (AppEn, *right*). Both are modulated by CLOSe phase-shift relative to *no stimulation* (dashed line) for *in silico* (*top*) and *in vitro* (*bottom*) data. **h** CoV (*left*) and AppEn (*right*) plotted against burst modulation for different CLOSe phase-shifts, averaged across all 10 mouse *in vitro* sessions. **i** Same but for the 4 NHP in vivo datasets. R and P values from linear correlation across phase-shifts.

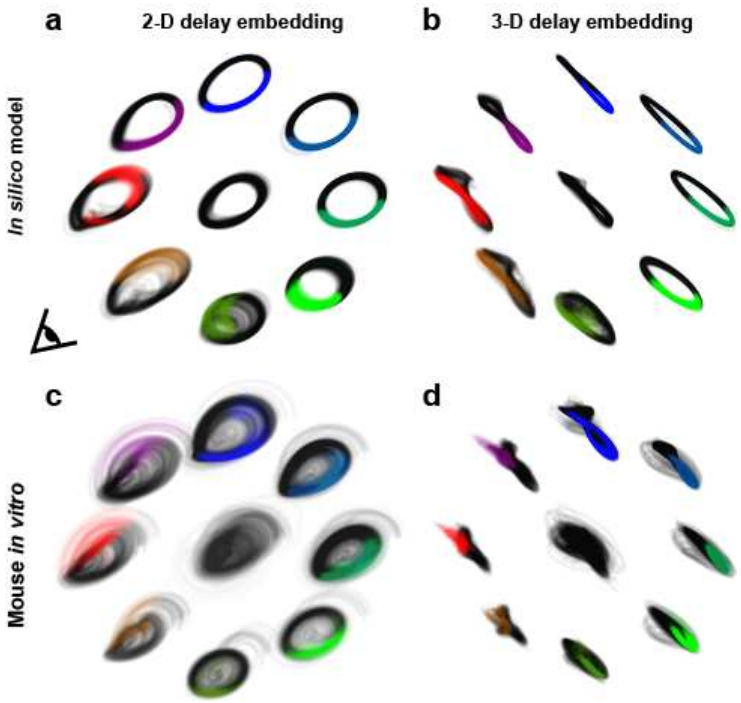

Supplemental Figure 5 – Seizure trajectories under different CLOSe phase-shifts *in silico* and *in vitro*. **a** 2-D delay-embedded LFP trajectories during seizure bursts for the *in silico* model under all CLOSe phase-shifts. Colour indicates when in the cycle stimulation was delivered. **b** 3-D trajectories viewed from angle indicated in panel a. **c**, **d** Same but for example mouse *in vitro* session.

Discussion

Over recent years, optogenetics has emerged as a powerful tool for manipulating neural populations with unprecedented spatial resolution and cell-type specificity. Our results highlight a further advantage of optical stimulation that is less widely appreciated, namely the ability for feedback control using concurrent electrical recordings without interference from artefacts, allowing for continuous, dynamic interaction with the neural tissue. We found that the effects of closed-loop, excitatory optogenetic stimulation depended critically on the timing relative to ongoing activity, with $CLOSe^{+}$ able to drive strong oscillations at a range of frequencies in quiescent tissue, and $CLOSe^{-}$ suppressing endogenous activity and pathological seizure-like oscillations. While optical stimulation is not free from potential sources of artefact (e.g. photoelectric effects), several lines of evidence point conclusively to an opsin-mediated effect in our data. First, we verified opsin expression and functionality from spike recordings and post-mortem histology (Supp. Fig. 2). Second, we saw no modulation when using light outside the absorption spectrum of our opsins (Fig. 2f). Third, the evoked responses exhibited polarity-reversals through the tissue, which resembled those of spontaneous activity (Supp. Fig. 3). Fourth, the modulatory effects of CLOSe depended consistently on the phase-shift relative to high-gamma activity rather the low-frequency LFP (Fig. 1d). Finally, optogenetic responses were attenuated with increasing frequency, as expected for physiological opsin activation (Boyden et al., 2005).

The ability to manipulate oscillatory activity systematically with CLOSe has many scientific applications for exploring the function of neural oscillations. While other interventions (e.g. pharmacological) can be used to enhance or block oscillations, an advantage of CLOSe is that enhancement and suppression at different frequencies can be interspersed within the same experimental design, simply by tuning parameters of the feedback loop (e.g. the filter pass-band and phase-shift). Moreover, potential uses extend beyond driving the predefined activity up, or down, since the addition of closed-loop feedback to a recurrent network can qualitatively alter the dynamics expressed by that system. For example, we showed computational and experimental evidence that CLOSe altered the sensitivity of state-space limit cycles to noise perturbations, thus precipitating or delaying phase transitions to non-oscillatory states. We used a relatively simple feedback algorithm, but the combination of nonlinear control theory (Taylor et al., 2015, Tang and Bassett, 2018) with closed-loop optogenetic paradigms offers new possibilities to both to test hypotheses about the role of phase transitions and metastability in brain function and behaviour (Tognoli and Kelso, 2014, Deco et al., 2019). Closed-loop stimulation may also influence network dynamics on longer time-scales, for example by influencing associative plasticity mechanisms (Jackson et al., 2006, Zanos et al., 2018).

In future, these approaches may extend the scope of current neurostimulation treatments. For epilepsy, responsive electrical stimulators can intervene upon detection of seizure onset (Skarpaas et al., 2019). At present, these interventions comprise open-loop trains of stimuli, but theoretical work suggests the effect of stimulation may depend on its timing of stimulation relative to activity cycles (Suffczynski et al., 2004, Taylor et al., 2014). In rodents, there is evidence that closed-loop electrical stimulation which takes into account the phase of the seizure cycle can be more effective than open-loop stimulation (Berényi et al., 2012). Similarly, adaptive DBS for Parkinson's disease is being trialled in humans, but this is currently limited to adjusting the amplitude of open-loop stimulation (Arlotti et al., 2018). However, phase-dependent electrical stimulation delivered to the globus pallidus has recently been used to disrupt pathological oscillations recorded in the overlying cortex of rodents (McNamara et al., 2020), while optogenetics would allow such stimulation to be controlled in real-time by abnormal activity recorded from the local network without interference from artefacts. Optogenetic therapies for epilepsy have been demonstrated in rodent models, but thus far these

consist of continuous inhibitory stimulation delivered once a seizure is detected (Paz et al., 2013, Krook-Magnuson et al., 2013). We chose to test excitatory stimulation in part because inhibition-based strategies are difficult to translate to humans. Ion-pumps like halorhodopsin (Paz et al., 2013) are relatively inefficient and require high light levels to inhibit neuronal activity, while high expression of excitatory opsins in inhibitory neurons (Krook-Magnuson et al., 2013) is difficult to drive with viral methods (although see (Vormstein-Schneider et al., 2020)). Moreover, some epilepsies are associated with a loss of interneuron populations (de Lanerolle et al., 1989, Andrioli et al., 2007), while in other cases, interneuronal activity may even induce seizure activity (Ledri et al., 2014, Magloire et al., 2019). A major consideration here, is that control of epileptic activity by GABAergic inhibition, or hyperpolarising ion channels like ACR, relies on appropriate chloride gradients being maintained during seizures, which may not be the case in practice (Alfonsa et al., 2015). As might be expected from an excitatory opsin, CLOSe was generally more effective at enhancing rather than suppressing oscillations, although both were possible with the appropriate phase-shift. Nevertheless, given the above considerations, it is likely that the effect of inhibitory stimulation may also depend on the instantaneous network state. Thus, closed-loop optogenetics may also benefit seizure-suppression strategies using inhibitory opsins by allowing more effective suppression with less overall light delivered, but this remains to be tested experimentally.

Several major challenges face the translation of optogenetics to the human brain. First, is to demonstrate the safety and efficacy of opsin expression. The use of viral vectors in primates has lagged somewhat behind the progress being made in rodents, but our study is among several to show that widespread, high expression levels can be obtained (Diester et al., 2011, Yazdan-Shahmorad et al., 2016). Optogenetic control of human neurons has been demonstrated in organotypic cultures (Andersson et al., 2016), but more work is needed to assess the potential risks of long-term expression of opsins (Shen et al., 2020). Second, a safe method of delivering sufficient light is required without the infection risk posed by percutaneous light fibres. We demonstrated that effective modulation of local brain activity in non-human primate could be obtained using implanted LEDs. Long-term protection of active electronic components within brain tissue is a challenge but the silicone encapsulation technique we used here has proven to be highly reliable in accelerated lifetime testing of insulators (Lamont, 2020). We are currently developing array implants that combine multiple forks with multiple LEDs on each prong to deliver uniform or patterned illumination to a large volume of cortex, together with custom CMOS circuitry (Ramezani et al., 2018) to process LFP recordings, supply drive current and monitor LED temperature (Dehkhoda et al., 2018). The cell-specific control enabled by optogenetics has applications in many neurological disorders, and we hope these technologies will help translate the promise of optogenetic therapies to the human brain.

Methods

All animal procedures were carried out under appropriate licenses issued by the UK Home Office under the Animals (Scientific Procedures) Act 1986, and were approved by the Animal Welfare and Ethical Review Board of Newcastle University.

In vitro mouse experiments

Brain slices were prepared from male C57BL/6J mice expressing channelrhodopsin in pyramidal neurons. Cell-specific expression was achieved by crossing mice homozygous for Cre-recombinase under the Emx1 promoter (EMX1-IRES-Cre mice; Stock #005628, The Jackson Laboratory, USA) with mice carrying the floxed channelrhodopsin gene (Ai19-flox-channelrhodopsin; Jackson Stock #12569). Young adult mice were anesthetized with isoflurane prior to intramuscular injection of ketamine (≥100 mg kg^{-1}) and xylazine (≥10 mg kg^{-1}) and intracardial perfusion with modified artificial cerebrospinal fluid (ACSF) composed of (mM) 252 sucrose, 3.0 KCl, 1.25 NaH_2PO_4, 24 $NaHCO_3$, 2.0 $MgSO_4$, 2.0 $CaCl_2$ and 10 glucose. Following brain removal, 450 µm horizontal slices were cut with a vibratome and transferred to a holding chamber at room temperature for approximately 1 hr. They were then placed in a recording chamber at the interface of normal ACSF (sucrose replaced with 126 mM NaCl) maintained at 32–34 °C and humidified with 95% O_2/5% CO_2. Multielectrode arrays (A16x1-2mm-100-177, NeuroNexus) were used to record LFPs (connected to either a Multichannel Systems MP8I headstage, PGA amplifier and CED Micro1401 running Spike2 v7, or an INTAN RHD2000 running v2 software). Optical stimulation was delivered via a 200 µm ferule (M89L01–200, Thorlabs) positioned 40mm above the slice. This was connected via a fibre optic cable to LED cubes delivering either a blue (470 nm, M470F1, Thorlabs to activate the opsin) or yellow (590 nm, M590F2, Thorlabs as a control) LED driven up to a maximum current of 1.2 A (T-cube, ThorLabs). We report data from 21 sessions in quiescent brain slices, and 10 sessions in which seizure-like activity was induced by bath application of 200 mM 4-AP.

In vivo NHP experiments

Experiments were conducted in two female macaca mulatta monkeys (age 4.3-5.3 years, weight: 5.7-6.7 kg), coded Z and Y. The animals were injected with optogenetic viruses under anaesthesia (2% sevoflurane and alfentanil 0.2-0.3 µg/kg/min i.v.) and aseptic conditions. Methylprednisolone (30 mg/kg followed by 5.4 mg/kg/h i.v. infusion) was given to reduce oedema, together with subcutaneous injection of meloxicam (0.3 mg/kg). The injections were performed in the primary motor cortex (M1), following a craniotomy and dural resection to visualise the central sulcus. Z and Y both received AAV8-hSyn-Chronos-GFP (10^{12} VP/ml, University of North Carolina Vector Core, USA) in the right M1. Monkey Z was additionally injected with Lenti-hSyn-eYFP-2A-ChR2(H134R) (10^9 vp/ml, our construct, Vigene Biosciences) in the left M1 in a subsequent procedure. Injections used multiple stainless steel needles (diameter= 0.3 mm, 1 mm separation, Y: 4 needles, Z: 8 needles) connected to Hamilton syringes via tubing filled with silicone oil. The syringes were mounted on ultra-micro-pumps (UMP3) synchronously controlled with the SYS-Micro4 controller (World Precision Instruments). 5 µl of virus was injected per site at multiple depths from 1-4 mm below the cortical surface at either 500 nl/min (Y) or 250 nl/min (Z). The total volume of virus injected is given in Supp Table 1.

Monkey	Hemisphere	Virus	Quantity	Endogenous Datasets	Seizure datasets
Z	Right	AAV8-hSyn-Chronos-GFP	120 µl	Light fibre (f_{filt}=2,5,10,20,40 Hz)	Light fibre (f_{filt}=15 Hz) Implanted LED (f_{filt}=20 Hz)
Z	Left	Lenti-hSyn-eYFP-2A-ChR2(H134R)	80 µl	Light fibre (f_{filt}=2,5,10,20,40 Hz) Implanted LED (f=10 Hz)	Light fibre (f_{filt}=25 Hz)
Y	Right	AAV8-hSyn-Chronos-GFP	80 µl	Light fibre (f_{filt}=2,5,10,20,40 Hz)	Light fibre (f_{filt}=20 Hz)

Supplemental Table 1 – Endogenous and seizure activity datasets from three hemispheres of two monkeys (Z and Y)

Experiments were carried out under terminal anaesthesia in monkey Y (50 days after injection) and monkey Z (134 and 50 days after the injection of AAV-Chronos and Lenti-ChR2 respectively). Supp. Table. 1 details the datasets collected in each animal. Surgical preparation of the injection site was performed under inhalation anaesthesia (1-2% sevoflurane) after which we switched to intravenous infusion of ketamine (6 mg/kg/h), alfentanil (0.2-0.3 µg/kg/min) and midazolam (0.14 mg/kg/hr) in order to maintain cortical excitability. The animals were ventilated and hydrated, and heart rate, blood pressure, saturation, end-tidal CO_2 and temperature were monitored throughout.

Neural activity in monkey Y was recorded using a NeuroNexus probe (A4X1-tet-3mm-150-121) and in monkey Z using U-probes (260 µm shaft diameter, 32 channels, 100 µm linear spacing, Plexon Inc). Data were amplified and acquired at 25 kHz using the RHD2000 system (Intan Technologies). Light was delivered through a 200 µm ferule (M89L01–200, Thorlabs) inserted superficially into the cortex, mounted to the same LED cubes as used in the *in vitro* experiments. In some experiments in monkey Z, we additionally used an implanted LED (see section below) to deliver light to the tissue.

After collecting data based on endogenous activity, 4-AP (100 mM) was injected into the cortex using a Hamilton syringe and ultra-micro-pump (UMP3) with the SYS-Micro4 controller (World Precision Instruments). Multiple injections of 1 µl at 200 nl/min were made at the same site until sustained seizure activity was observed (typically 5-10 µl per hemisphere).

At the end of the experiment, monkeys were deeply anesthetized with propofol and transcardially perfused with phosphate-buffered saline followed by 4% paraformaldehyde. The brain tissue containing the injection/recording site was stereotaxically dissected and equilibrated in 30% sucrose before 20 µm horizontal sectioning. Antibodies for the fluorescent marker (anti-GFP ab290, anti-mCherry ab167453), neuronal nuclei markers (anti-NeuN, ab104224) and astroglia (anti-GFAP, ab4674, all Abcam) were used prior to upright fluorescence microscopy (Eclipse NiE, Nikon) and confocal imaging (LSM 800 Airyscan, Zeiss).

Implantable LED array

Supplemental Figure 4a shows the implantable optrode fork. Optrode fabrication began with a 200 µm-thick silicon wafer which underwent a standard solvent clean procedure in n-methyl pyrrolidine (NMP) followed by isopropanol (IPA) and then rinsed in deionised water. A 1 µm-thick insulation SiO_2 layer was deposited by chemical vapour deposition on the silicon surface. Ti/Au/Ti metallisation was deposited by evaporation on top of the insulation, and patterned by UV photolithography to outline the metal tracks and recording electrodes. Metal patterning was carried out by a selective wet etch based on NH_4OH:H_2O_2 (1:2) for titanium, and a $K_3Fe(CN)_6$, $Na_2S_2O_3$ and $CS(NH_2)_2$ in deionised water mixture for gold. The Ti/Au/Ti patterns were then capped with a second SiO_2 insulation layer. Contact windows through the top insulation needed to access the bonding pads were opened by reactive ion etch (RIE), using a Ti/Ni metal mask which was deposited by e-beam evaporation and patterned by UV photolithography and wet etching. Optrode singulation was achieved by deep reactive ion etching (DRIE).

Micro-LEDs (DA2432, Cree) were bonded on the gold LED pads on the optrode shaft using off-the-shelf Au/Sn preforms (Inseto, 100 µm x 100 µm x 10 µm, comparable with the LED footprint). Using a pick-and-place Fineplacer Lamda tool, a preform was placed on each of the two LED pads, the LED was placed directly on top of the AuSn preforms, and the LED/preforms stack was heated to 320°C to melt the preform and bond the LED.

The silicone rubber used for encapsulation was NuSIL MED6015, an optically clear, solvent free, low viscosity silicon elastomer safe for human implantation. The two-part rubber was mixed in a vortex mixer (10 part A:1 part B). The optrode surface was prepared by a solvent clean in acetone and IPA in an ultrasonic bath, then rinsed in deionised water. The optrodes were dipped into the silicone mix and then mounted on the vacuum holder of a spin coater. A uniform thickness of the silicone around the optrode was achieved by spinning at 2000 rpm for 5 seconds and 4000 rpm 10 seconds. The silicone was cured at 150°C for 15min.

The LED fork was inserted into the brain using a stereotaxic manipulator. We used a single LED at the tip of one shaft to deliver closed-loop stimulation. The LED was driven by a voltage-controlled constant current stimulator (DS4, Digitimer) up to a maximum current of 5mA. Supplemental Figure 4b compares the total light power emitted by the LED and the fibre-coupled Thorlab system over the full experimental range, measured using an integrating sphere (OPM150, Artifex Engineering). In both cases, the light source was placed near the centre of the integrating sphere, which captures light emitted from all angles into an integrated calibrated photodiode.

Closed-loop stimulation

The closed-loop algorithm was implemented in custom-designed hardware based around a dsPIC30F6012A microcontroller running at 30MHz. The microcontroller sampled the LFP from one electrode at 500 Hz, applied a causal phase-shifting finite impulse response (FIR) filter, thresholded (just above the background noise level) and half-wave rectified the output to generate a voltage signal which controlled the LED current driver. The FIR filter convolved the input signal with a 512 sample kernel given by:

$$kernal(t) = \alpha e^{k f_{filt} t} . \cos\left(2\pi f_{filt} t + \varphi\right) \quad \text{(Equ. 1)}$$

where t <0 (for a causal filter working on past signals only), k determines the filter band-width and was set to 1.25 for all experiments, φ determines the extent to which the output is phase-advanced from the input, and f_{filt} determines the central frequency of the pass-band. The amplitude and phase

response of this filter are shown in Figure 1a. In general, for our seizure experiments we chose f_{filt} to be the dominant frequency of the seizure bursts (in the range 10-20 Hz), and for non-seizure recordings, we chose frequencies between 2-40 Hz. The remaining free parameter, α, is an overall scaling factor that determines the light intensity for a given filter output. We adjusted this in advance such that endogenous activity would drive the LED over its full current range. Note however that once engaged, CLOSe$^+$ feedback often enhanced the oscillations such that the light pulses saturated at the maximum level.

CLOSe was delivered for epochs of fixed duration, each interspersed with an equal-duration epoch of no stimulation. We used phase-shifts, φ, from 0, 45°,…, 315° delivered in pseudorandomised order. We chose epoch durations between 5-120s depending on the experiment, ensuring our datasets contained at least two repeats of each phase-shift. For quiescent/endogenous experiments we tended to use short-duration epochs, while for seizure experiments we selected in advance a duration such that at least one seizure event would likely occur within each epoch. Our quiescent brain slice recordings lasted between 11-91 min (mean 51 min), while our seizure sessions lasted between 28-211 min (mean 93 min). Our endogenous recordings in NHPs lasted between 10-14 min (mean 11 min) while our seizure datasets lasted between 63-71 min (mean 67 min).

Data analysis

Data were analysed using custom scripts written in Matlab (Mathworks, USA) and used the *circ_stats* toolbox for circular statistics (Berens, 2009). All off-line filtering used 4-pole Butterworth filters passed in forward and reverse directions. LFP was down-sampled to 500 Hz after anti-alias filtering. Power spectra were compiled using Welch's method using overlapping windows of length 512 sample points. CLOSe phase-shifts were adjusted by the relative phase between the LFP and high-gamma (>100 Hz) envelope which was determined by applying a Hilbert transform to the cross-correlation of these signals (Supp. Fig. 1).

For data on quiescent mouse brain slices and endogenous activity in NHPs, we compiled power spectra of the LFP driving CLOSe for the entirety of stimulation/control epochs, and averaged power modulation around the closed-loop filter frequency (0.8-1.2f_{filt}). Additionally, for the NHP linear microelectrode datasets, we calculated the depth-profile of cycle-triggered averages of the other LFPs, aligned to troughs in the band-pass filtered (0.8-1.2f_{filt}) channel that was driving CLOSe.

Seizure events in mouse brain slices occurred sporadically and were readily distinguished from quiet inter-ictal periods so we restricted our analysis to time-windows encompassing these events. The start times of these windows were identified using an appropriate threshold on the rectified LFP (typically 0.05-0.15 mV) and we calculated power spectra for a fixed duration that encompassed all the seizure bursts (typically around 20s). Within these windows, we additionally defined individual bursts as periods during which the rectified LFP was not less than threshold for more than 0.2 s, and excluded events with a duration less than 0.2 s. Typically the first burst within each seizure event was longer than subsequent bursts. Therefore, when computing the ratio of burst lengths under CLOSe to the no stimulation condition, we calculated this separately for first and subsequent bursts, before averaging over all bursts.

The seizure events in NHPs occurred more frequently and regularly, and it was not always possible to demarcate their onset from background activity. Therefore, we computed power spectra over the entirety of stimulation/control epochs for these data. To obtain a measure of seizure magnitude, we computed the amplitude envelope of the LFP (band-pass filtered 10-30 Hz, rectified, and smoothed

with a 1 s Hanning window) and corrected for baseline activity by subtracting the mode average of this envelope. We then computed the autocorrelation function of this signal, which provides a visualisation of the temporal profile of seizure bursts. We quantified seizure magnitude from the area under this autocorrelation function (from -20 to +20 s). Note, however, that while the autocorrelation function reveals the temporal profile of seizure bursts (i.e. the width of the peak reflects the duration of seizures), the area under this peak provides a composite measure that is also influenced by the number and duration of seizure bursts as well as their individual amplitudes.

For the seizure datasets, we additionally calculated two metrics designed to quantify the stability of seizure cycles revealed by delay-embedded, band-pass filtered (*in vitro*: 5-30 Hz, *in vivo*: 10-30 Hz) LFP trajectories. We chose an embedding dimension of three, and obtained the optimal embedding delay from the average mutual information algorithm implemented by the Matlab function *phaseSpaceReconstruction* with default settings. Our first metric was geometric in nature and designed to assess variations in the instantaneous scalar radius of the three-dimensional trajectory (from the origin). We calculated the mean, $\mu(t)$, and standard deviation, $\sigma(t)$, of this radius using a sliding window of 100 ms width through time. We then defined a trajectory Coefficient of Variation (CoV) as the proportional relationship between these:

$$\sigma(t) = \mathrm{CoV} \times \mu(t) \qquad \text{(Equ. 2)}$$

CoV was calculated by least-squares fit of Equ. 2 over time. We chose this regression approach (rather than calculating $\sigma(t)/\mu(t)$ and averaging over time) to avoid our result being skewed by quiescent epochs with low values of $\mu(t)$. Our second metric was approximate entropy (AppEn) which is an information-theoretic measure of unpredictability in time series. This was calculated using the Matlab function *approximateEntropy* with the default similarity criterion of 0.2 times the standard deviation.

The modulation of all-positive metrics (LFP power, seizure burst duration/magnitude, trajectory stability) relative to *no-stimulation* was analysed using log-transformed ratios (i.e. a doubling/halving of seizure magnitude was treated as an equal and opposite modulation). We calculated the max/min modulation both for the raw datasets (i.e. selecting the phase-shift that yielded the largest average effect), and for a sinusoidal fit through all phase-shifts in the dataset. The former may overestimate the modulation due to variability inherent in each measurement and the latter may underestimate modulation if the data is not well fit by a sinusoid; therefore we show both values throughout. Additionally, we averaged our measures across datasets (aligned by adjusted phase-shift) and assessed the statistical significance of phase-dependent modulation using circular-linear correlation (CircStats Matlab toolbox).

Modelling

We used a simple two-population variant of the Wilson-Cowan neural population model, which has been described in detail in previous publications (Wang et al., 2012, Wang et al., 2014). The model comprised a single excitatory population and a single inhibitory population evolving according to the following differential equations:

$$\frac{dE}{dt} = \big(-E(t) + \mathrm{Sigm}(a \times E(t) - b \times I(t) + S(t) + P)\big)/\tau_e + \eta_e(t)$$

$$\frac{dI}{dt} = \big(-I(t) + \mathrm{Sigm}(c \times E(t) - d \times I(t) + Q)\big)/\tau_i + \eta_i(t) \qquad \text{(Equ. 3)}$$

where $E(t)$ and $I(t)$ are the activity of the excitatory and inhibitory neural populations at time t. The parameters a, b, c and d determine the strength of interaction between these populations, decaying with time constants τ_e and τ_i. This system additionally is subject to tonic drive, P and Q, and Gaussian noise inputs, $\eta_e(t)$ and $\eta_i(t)$ reflecting synaptic noise and inputs from the surrounding tissue. The LFP was modelled as a combination of the activity of both neuronal populations, which was fed in to the same closed-loop feedback algorithm as used in the experiments. Optical stimulation acted as an additional input, $S(t)$, to the excitatory neuronal population. Finally, the sigmoid function is:

$$\mathrm{Sigm}(x) = \frac{1}{1+e^{-x-4}} \qquad \text{(Equ. 4)}$$

We used the Euler-Maruyama method to simulate this system with a 1 ms time-step. Parameters used for the simulations are shown in Supp. Table 2, putting the system in a bistable state regime where a limit cycle coexists with the lower fixed point.

Parameter	Value
a	17
b	10
c	40
d	0
τ_e	0.0264
τ_i	0.012
P	-0.3
Q	-15

Supplemental Table 2 – Model parameters used for *in silico* simulations

Code and data availability statement

All data, analysis code and modelling code is available on request to the corresponding author (andrew.jackson@ncl.ac.uk). We intend to make data and code available on suitable repositories prior to publication of this manuscript.

Supplemental Movie 1 – Model trajectories with different CLOSe phase-shifts. *Left:* Phase-space plots of model attractor under CLOSe with different phase-shifts. *Right:* Attractor reconstructed from delay-embedded LFP simulation. Blue line indicates time of stimulation. Video shows two complete cycles of phase-shift. Note that as the phase-shift transitions from $CLOSe^+$ to $CLOSe^-$ the attractor first undergoes period doubling before becoming increasingly complex.

Acknowledgements

The project CANDO (Controlling Abnormal Network Dynamics with Optogenetics) is co-funded by the Wellcome Trust (102037) and Engineering and Physical Sciences Research Council (A000026). We thank all members of the CANDO consortium (www.cando.ac.uk). AJ is a Wellcome Trust Senior Research Fellow (106149).

Author contributions

In vitro experiments were performed and analysed by AH, MT, FELB, MOC, AJT and AJ. *In vivo* experiments were performed and analysed by BZ, MT, SNB and AJ. Virus development, testing and post-mortem histology was performed by CGdS and GJC. *In silico* simulations were performed by YW, FH, MK and AJ. The closed-loop algorithm was developed by SB and AJ. The optrode was designed and manufactured by EE-C, ASI, RB, ST, AP, NP, ND, TGC, PD and AON. AJ wrote the manuscript with input from all authors.

ALFONSA, H., MERRICKS, E. M., CODADU, N. K., CUNNINGHAM, M. O., DEISSEROTH, K., RACCA, C. & TREVELYAN, A. J. 2015. The contribution of raised intraneuronal chloride to epileptic network activity. *J Neurosci,* 35**,** 7715-26.

ANDERSSON, M., AVALIANI, N., SVENSSON, A., WICKHAM, J., PINBORG, L. H., JESPERSEN, B., CHRISTIANSEN, S. H., BENGZON, J., WOLDBYE, D. P. & KOKAIA, M. 2016. Optogenetic control of human neurons in organotypic brain cultures. *Sci Rep,* 6**,** 24818.

ANDRIOLI, A., ALONSO-NANCLARES, L., ARELLANO, J. I. & DEFELIPE, J. 2007. Quantitative analysis of parvalbumin-immunoreactive cells in the human epileptic hippocampus. *Neuroscience,* 149**,** 131-43.

ARLOTTI, M., MARCEGLIA, S., FOFFANI, G., VOLKMANN, J., LOZANO, A. M., MORO, E., COGIAMANIAN, F., PRENASSI, M., BOCCI, T., CORTESE, F., RAMPINI, P., BARBIERI, S. & PRIORI, A. 2018. Eight-hours adaptive deep brain stimulation in patients with Parkinson disease. *Neurology,* 90**,** e971-e976.

BERENS, P. 2009. CircStat: A MATLAB Toolbox for Circular Statistics. *Journal of Statistical Software,* 31.

BERÉNYI, A., BELLUSCIO, M., MAO, D. & BUZSÁKI, G. 2012. Closed-loop control of epilepsy by transcranial electrical stimulation. *Science,* 337**,** 735-7.

BOUTHOUR, W., MÉGEVAND, P., DONOGHUE, J., LÜSCHER, C., BIRBAUMER, N. & KRACK, P. 2019. Biomarkers for closed-loop deep brain stimulation in Parkinson disease and beyond. *Nat Rev Neurol,* 15**,** 343-352.

BOYDEN, E. S., ZHANG, F., BAMBERG, E., NAGEL, G. & DEISSEROTH, K. 2005. Millisecond-timescale, genetically targeted optical control of neural activity. *Nat Neurosci,* 8**,** 1263-8.

CAGNAN, H., DENISON, T., MCINTYRE, C. & BROWN, P. 2019. Emerging technologies for improved deep brain stimulation. *Nat Biotechnol,* 37**,** 1024-1033.

DE LANEROLLE, N. C., KIM, J. H., ROBBINS, R. J. & SPENCER, D. D. 1989. Hippocampal interneuron loss and plasticity in human temporal lobe epilepsy. *Brain Res,* 495**,** 387-95.

DECO, G., CRUZAT, J., CABRAL, J., TAGLIAZUCCHI, E., LAUFS, H., LOGOTHETIS, N. K. & KRINGELBACH, M. L. 2019. Awakening: Predicting external stimulation to force transitions between different brain states. *Proc Natl Acad Sci U S A,* 116**,** 18088-18097.

DEHKHODA, F., SOLTAN, A., PONON, N., JACKSON, A., O'NEILL, A. & DEGENAAR, P. 2018. Self-sensing of temperature rises on light emitting diode based optrodes. *J Neural Eng,* 15**,** 026012.

DIESTER, I., KAUFMAN, M. T., MOGRI, M., PASHAIE, R., GOO, W., YIZHAR, O., RAMAKRISHNAN, C., DEISSEROTH, K. & SHENOY, K. V. 2011. An optogenetic toolbox designed for primates. *Nat Neurosci,* 14**,** 387-97.

GROSENICK, L., MARSHEL, J. H. & DEISSEROTH, K. 2015. Closed-loop and activity-guided optogenetic control. *Neuron,* 86**,** 106-39.

HALL, T. M., NAZARPOUR, K. & JACKSON, A. 2014. Real-time estimation and biofeedback of single-neuron firing rates using local field potentials. *Nat Commun,* 5**,** 5462.

JACKSON, A., MAVOORI, J. & FETZ, E. E. 2006. Long-term motor cortex plasticity induced by an electronic neural implant. *Nature,* 444**,** 56-60.

KROOK-MAGNUSON, E., ARMSTRONG, C., OIJALA, M. & SOLTESZ, I. 2013. On-demand optogenetic control of spontaneous seizures in temporal lobe epilepsy. *Nat Commun,* 4**,** 1376.
LAMONT, C. 2020. Non-Hermetic Protection of Thin-Film Metallisation Layers Intended for Implanted Electronic Medical Devices. *Doctoral thesis (Ph.D), UCL (University College London).*
LEDRI, M., MADSEN, M. G., NIKITIDOU, L., KIRIK, D. & KOKAIA, M. 2014. Global optogenetic activation of inhibitory interneurons during epileptiform activity. *J Neurosci,* 34**,** 3364-77.
LITTLE, S., POGOSYAN, A., NEAL, S., ZAVALA, B., ZRINZO, L., HARIZ, M., FOLTYNIE, T., LIMOUSIN, P., ASHKAN, K., FITZGERALD, J., GREEN, A. L., AZIZ, T. Z. & BROWN, P. 2013. Adaptive deep brain stimulation in advanced Parkinson disease. *Ann Neurol,* 74**,** 449-57.
MAGLOIRE, V., MERCIER, M. S., KULLMANN, D. M. & PAVLOV, I. 2019. GABAergic Interneurons in Seizures: Investigating Causality With Optogenetics. *Neuroscientist,* 25**,** 344-358.
MCNAMARA, C. G., ROTHWELL, M. & SHAROTT, A. 2020. Phase-dependent closed-loop modulation of neural oscillations in vivo. *bioRxiv***,** 2020.05.21.102335.
NICHOLSON, E., KUZMIN, D. A., LEITE, M., AKAM, T. E. & KULLMANN, D. M. 2018. Analogue closed-loop optogenetic modulation of hippocampal pyramidal cells dissociates gamma frequency and amplitude. *Elife,* 7.
PAZ, J. T., DAVIDSON, T. J., FRECHETTE, E. S., DELORD, B., PARADA, I., PENG, K., DEISSEROTH, K. & HUGUENARD, J. R. 2013. Closed-loop optogenetic control of thalamus as a tool for interrupting seizures after cortical injury. *Nat Neurosci,* 16**,** 64-70.
RAMEZANI, R., LIU, Y., DEHKHODA, F., SOLTAN, A., HACI, D., ZHAO, H., FIRFILIONIS, D., HAZRA, A., CUNNINGHAM, M. O., JACKSON, A., CONSTANDINOU, T. G. & DEGENAAR, P. 2018. On-Probe Neural Interface ASIC for Combined Electrical Recording and Optogenetic Stimulation. *IEEE Trans Biomed Circuits Syst,* 12**,** 576-588.
SHANECHI, M. M. 2019. Brain-machine interfaces from motor to mood. *Nat Neurosci,* 22**,** 1554-1564.
SHEN, Y., CAMPBELL, R. E., CÔTÉ, D. C. & PAQUET, M. E. 2020. Challenges for Therapeutic Applications of Opsin-Based Optogenetic Tools in Humans. *Front Neural Circuits,* 14**,** 41.
SIEGLE, J. H. & WILSON, M. A. 2014. Enhancement of encoding and retrieval functions through theta phase-specific manipulation of hippocampus. *Elife,* 3**,** e03061.
SKARPAAS, T. L., JAROSIEWICZ, B. & MORRELL, M. J. 2019. Brain-responsive neurostimulation for epilepsy (RNS(®) System). *Epilepsy Res,* 153**,** 68-70.
SOHAL, V. S., ZHANG, F., YIZHAR, O. & DEISSEROTH, K. 2009. Parvalbumin neurons and gamma rhythms enhance cortical circuit performance. *Nature,* 459**,** 698-702.
STARK, E., ROUX, L., EICHLER, R., SENZAI, Y., ROYER, S. & BUZSÁKI, G. 2014. Pyramidal cell-interneuron interactions underlie hippocampal ripple oscillations. *Neuron,* 83**,** 467-480.
SUFFCZYNSKI, P., KALITZIN, S. & LOPES DA SILVA, F. H. 2004. Dynamics of non-convulsive epileptic phenomena modeled by a bistable neuronal network. *Neuroscience,* 126**,** 467-84.
TANG, E. & BASSETT, D. S. 2018. Colloquium: Control of dynamics in brain networks. *Reviews of Modern Physics,* 90**,** 031003.
TAYLOR, P. N., THOMAS, J., SINHA, N., DAUWELS, J., KAISER, M., THESEN, T. & RUTHS, J. 2015. Optimal control based seizure abatement using patient derived connectivity. *Front Neurosci,* 9**,** 202.
TAYLOR, P. N., WANG, Y., GOODFELLOW, M., DAUWELS, J., MOELLER, F., STEPHANI, U. & BAIER, G. 2014. A computational study of stimulus driven epileptic seizure abatement. *PLoS One,* 9**,** e114316.
TOGNOLI, E. & KELSO, J. A. 2014. The metastable brain. *Neuron,* 81**,** 35-48.
UHLHAAS, P. J. & SINGER, W. 2006. Neural synchrony in brain disorders: relevance for cognitive dysfunctions and pathophysiology. *Neuron,* 52**,** 155-68.
VORMSTEIN-SCHNEIDER, D., LIN, J. D., PELKEY, K. A., CHITTAJALLU, R., GUO, B., ARIAS-GARCIA, M. A., ALLAWAY, K., SAKOPOULOS, S., SCHNEIDER, G., STEVENSON, O., VERGARA, J., SHARMA, J., ZHANG, Q., FRANKEN, T. P., SMITH, J., IBRAHIM, L. A., M ASTRO, K. J., SABRI, E., HUANG, S., FAVUZZI, E., BURBRIDGE, T., XU, Q., GUO, L., VOGEL, I., SANCHEZ, V., SALDI, G. A., GORISSEN, B. L., YUAN, X., ZAGHLOUL, K. A., DEVINSKY, O., SABATINI, B. L., BATISTA-BRITO, R., REYNOLDS,

J., FENG, G., FU, Z., MCBAIN, C. J., FISHELL, G. & DIMIDSCHSTEIN, J. 2020. Viral manipulation of functionally distinct interneurons in mice, non-human primates and humans. *Nature Neuroscience*.

WANG, Y., GOODFELLOW, M., TAYLOR, P. N. & BAIER, G. 2012. Phase space approach for modeling of epileptic dynamics. *Phys Rev E Stat Nonlin Soft Matter Phys,* 85**,** 061918.

WANG, Y., GOODFELLOW, M., TAYLOR, P. N. & BAIER, G. 2014. Dynamic mechanisms of neocortical focal seizure onset. *PLoS Comput Biol,* 10**,** e1003787.

YAZDAN-SHAHMORAD, A., DIAZ-BOTIA, C., HANSON, T. L., KHARAZIA, V., LEDOCHOWITSCH, P., MAHARBIZ, M. M. & SABES, P. N. 2016. A Large-Scale Interface for Optogenetic Stimulation and Recording in Nonhuman Primates. *Neuron,* 89**,** 927-39.

ZANOS, S., REMBADO, I., CHEN, D. & FETZ, E. E. 2018. Phase-Locked Stimulation during Cortical Beta Oscillations Produces Bidirectional Synaptic Plasticity in Awake Monkeys. *Curr Biol,* 28**,** 2515-2526.e4.

ZHOU, Y., HUANG, R., CHEN, Z., CHANG, X., CHEN, J. & XIE, L. 2012. Application of approximate entropy on dynamic characteristics of epileptic absence seizure. *Neural Regen Res,* 7**,** 572-7.

Figures

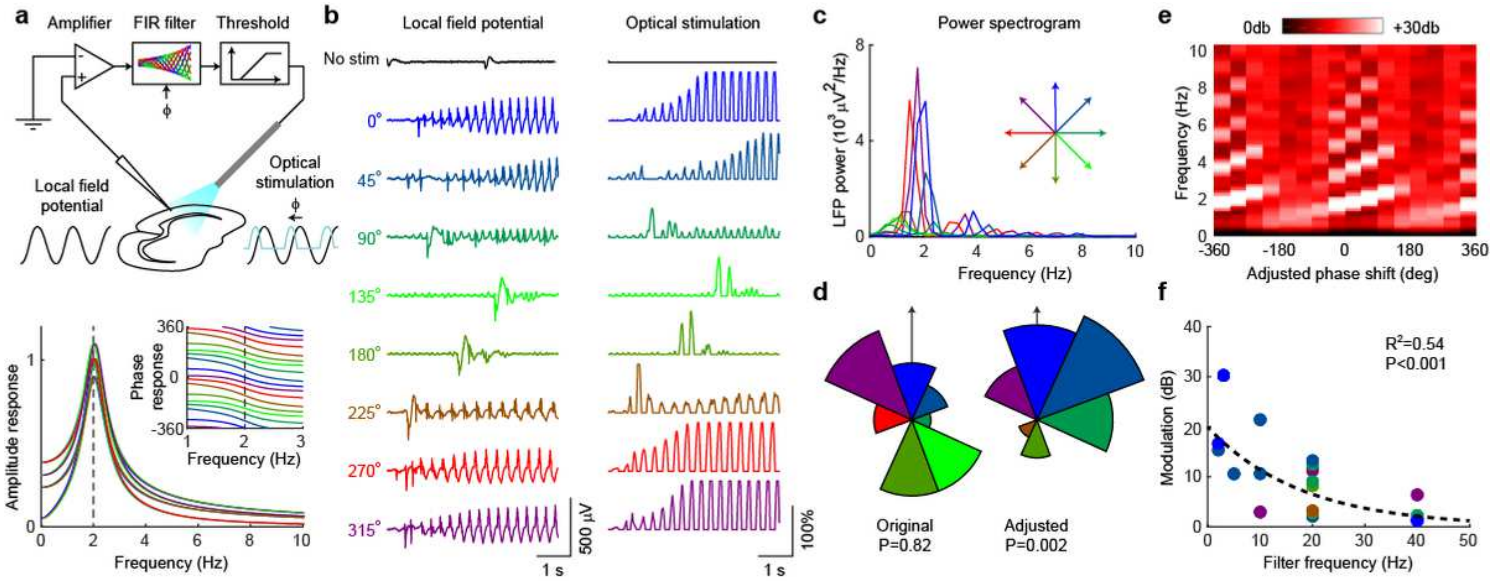

Figure 1

CLOSe drives oscillations in quiescent mouse brain slices. a Top: Schematic of experimental setup. LFP, recorded from an Emx1-ChR2 mouse, brain slice was filtered and used to control optical stimulation in real-time. Bottom: Amplitude response of filter. Inset shows phase response across the passband. b Example LFP and stimulation traces under no stimulation (black) and CLOSe with different phase-shifts (relative to LFP, 2 Hz filter frequency). c LFP power spectra for different phase-shifts. d Left: Phase-shifts (relative to LFP) associated with maximal oscillation in 21 sessions. Right: Adjusted phase-shifts (relative to high gamma activity; see Supp. Fig. 1). P values from Rayleigh test for circular non-uniformity. e LFP power at different frequencies for different adjusted phase-shifts (2 Hz filter). Phase-shift is unwrapped and plotted over two cycles. f Phase-dependent modulation of LFP power for different filter frequencies. Colour indicates adjusted phase-shift associated with maximal oscillation. Dashed line shows log-linear fit to data.

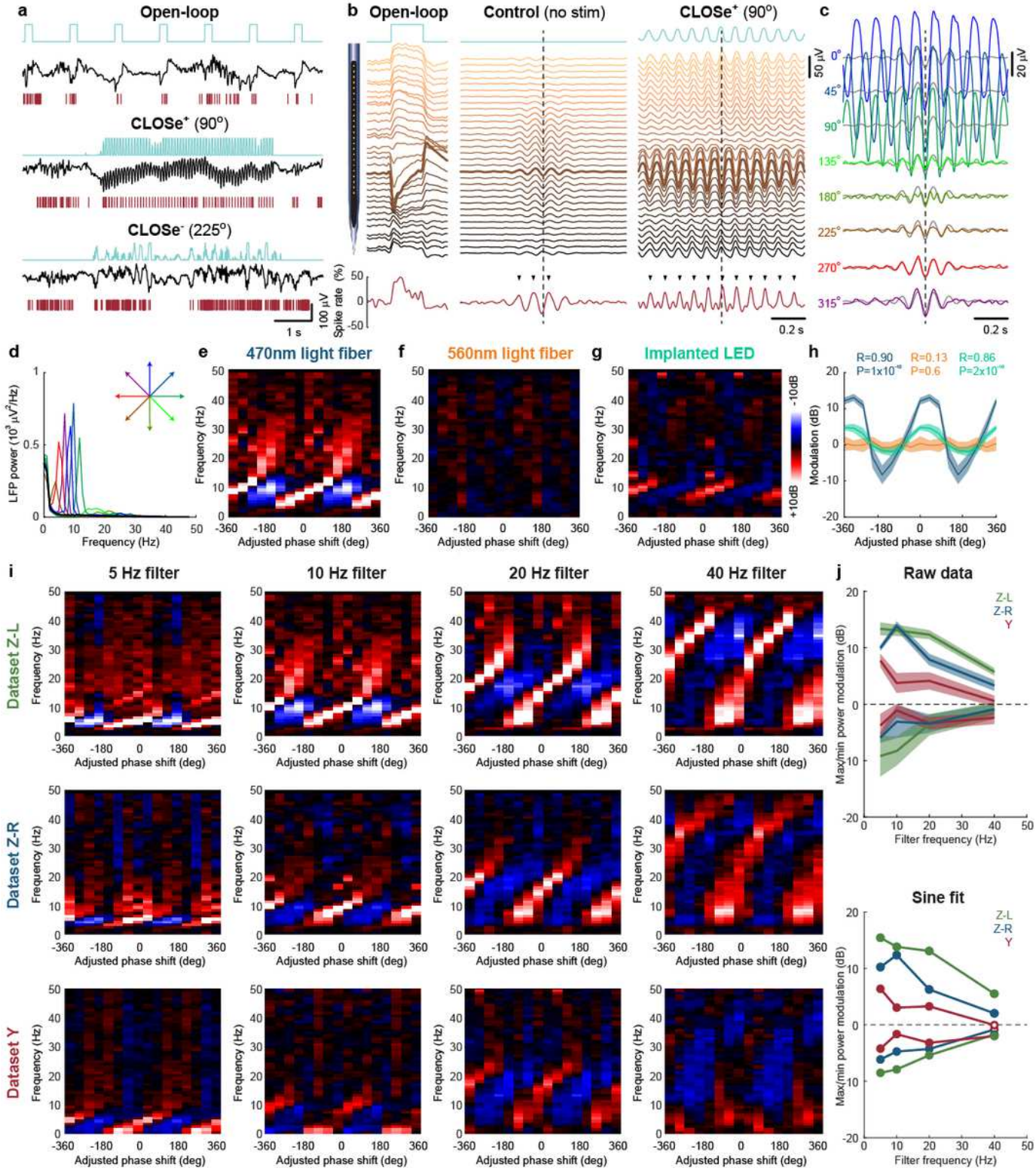

Figure 2

CLOSe modulates endogenous activity in vivo in non-human primates. a Example LFP and spike activity during open-loop stimulation and 5 s CLOSe epochs with two different phase-shifts (10 Hz filter) recorded from monkey motor cortex injected with Lenti-hSyn-eYFP-2A-ChR2(H134R). b Left: Stimulus-triggered average LFP and neural response to open-loop stimulation. Stacked traces indicate LFP recorded from different electrodes on the linear array (3 mm total). The thick line indicates LFP used for CLOSe. Multiple

phase reversals are evident in the response. Right: LFP cycle-triggered averages (aligned to troughs in the CLOSe LFP, dashed line) during no stimulation and CLOSe+. Tick marks indicate significant increased spike rate (average of 21 cells) compared to shuffled surrogates. Note that the LFP phase reversal observed in the endogenous activity matches that driven by optical stimulation. c Cycle-triggered averages for all CLOSe phase-shifts. Note that CLOSe¬- reduced the amplitude of LFP cycles relative to no stimulation (grey traces). d LFP power spectra for epochs of CLOSe with different phase-shifts. e Relative power modulation for different CLOSe phase-shifts, showing frequencies with increased (red) and reduced (blue) activity relative to no stimulation. f No modulation was observed when stimulating with a frequency of light outside the opsin absorption range. g LFP modulation driven by an implanted LED. h LFP modulation (between 0.8-1.2x the filter frequency) for the three datasets. R and P values from circular-linear correlation over stimulation epochs. i LFP modulation for different filter frequencies replicated in three datasets (Z-L: Lenti-hSyn-eYFP-2A-ChR2(H134R); Z-R and Y: AAV8-hSyn-Chronos-GFP). j Maximum/minimum power modulation (between 0.8-1.2x the filter frequency) for different filter frequencies. Top: maximum/minimum value for any phase-shift. Shading indicates s.e.m. over stimulation epochs. Bottom: maximum/minimum values of sinusoidal fit to data. Filled circles indicate significant phase-dependent modulation (circular-linear correlation over stimulus epochs, P<0.05).

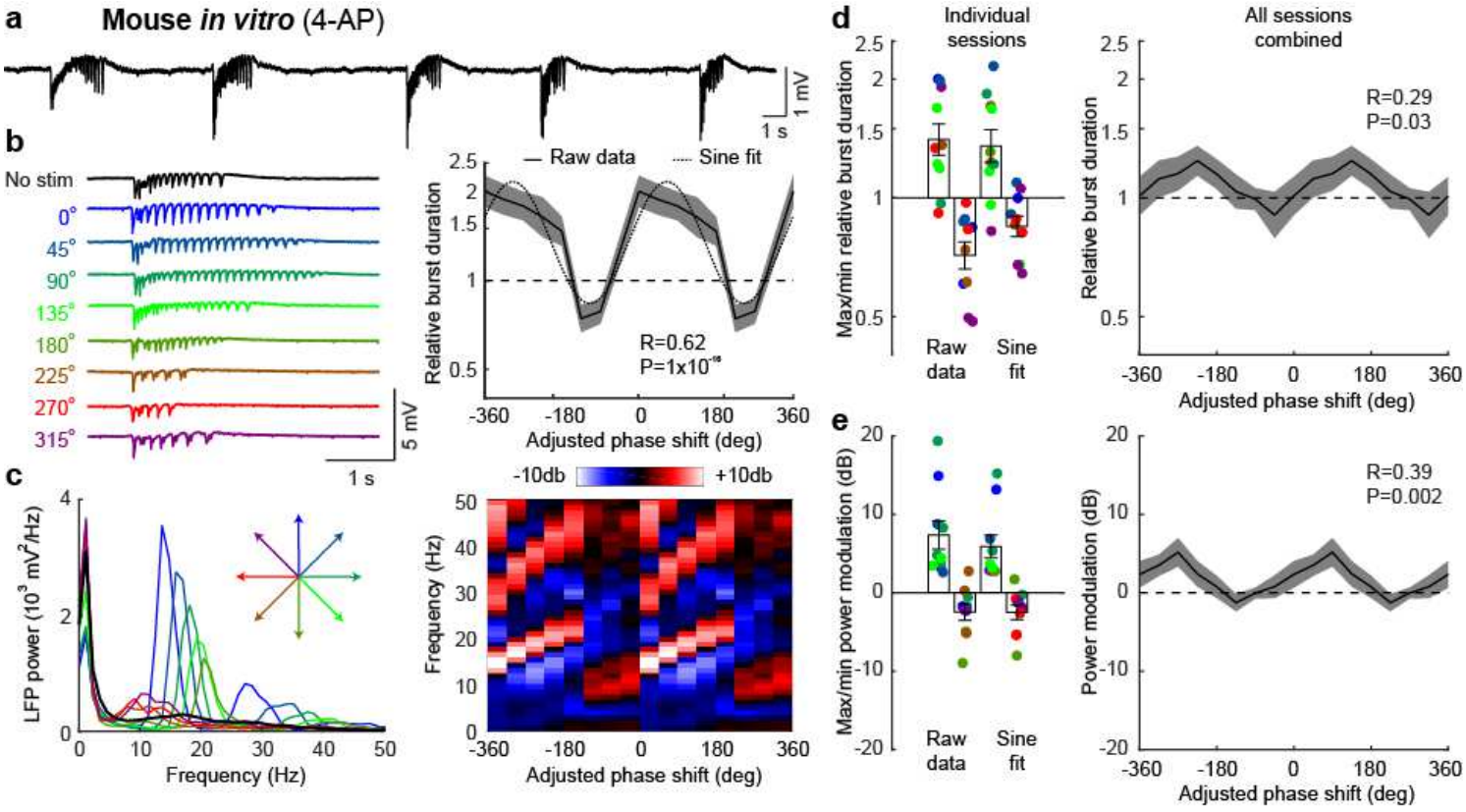

Figure 3

CLOSe modulates 4AP-induced epileptiform activity in mouse brain slices. a Example seizure-like event comprising multiple bursts elicited by bath application of 4-AP to Emx-ChR2 mouse brain slices. b Left: Individual seizure bursts under CLOSe (20 Hz filter) with different phase-shifts showing phase-dependent prolongation and shortening of burst duration. Right: Average burst duration relative to no stimulation for

different CLOSe phase-shifts. Shading indicates s.e.m. over bursts. R and P values from circular-linear correlation over bursts. Dashed line shows sinusoidal fit. c Left: LFP power spectra during seizure-like events under different CLOSe phase-shifts. Right: Modulation of LFP power relative to no stimulation. d Left: Max/min modulation of burst duration across 10 sessions for raw data and sinusoidal fit. Colour shows phase-shift associated with max/min for individual sessions. Right: Average modulation of burst duration averaged across sessions. e Same but for LFP power at seizure frequency. Error bars indicate s.e.m. over sessions. R and P values from circular linear correlation over datasets.

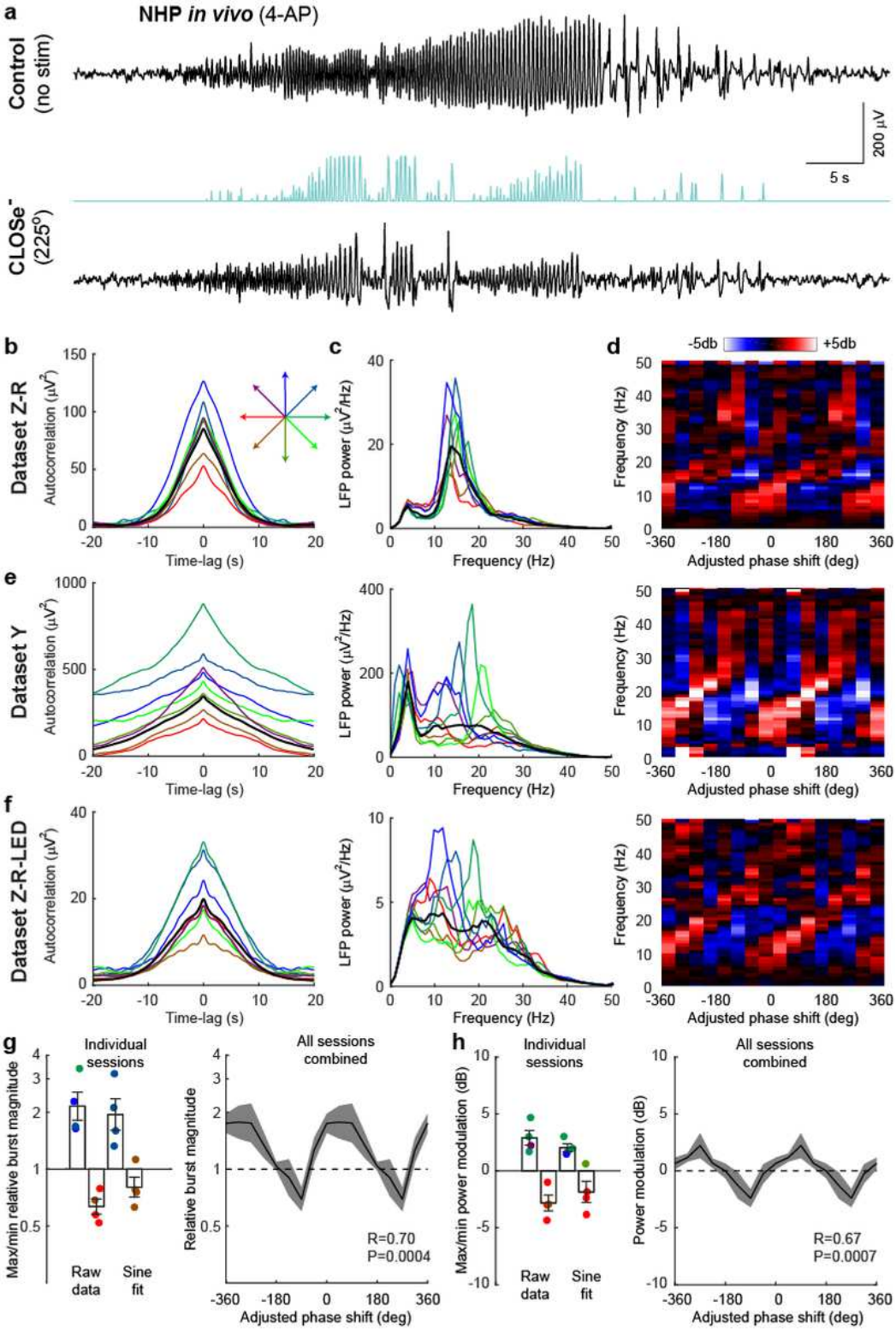

Figure 4

CLOSe modulates 4AP-induced epileptiform activity in vivo in non-human primates. a Top: Example seizure-like event elicited by intracortical injection of 4-AP in monkey motor cortex. Bottom: Example seizure-like event under CLOSe- (15 Hz filter frequency). b Autocorrelation of seizure-band LFP amplitude envelope reveals temporal structure of seizure burst under no stimulation (black). Coloured traces show modulation by CLOSe with different phase-shifts. c Left: LFP power spectra under different CLOSe phase-shifts. Right: Modulation of LFP power relative to no stimulation. e Same for replication in a second animal. f Same for replication using implanted LED to deliver light. g Left: Max/min modulation of burst magnitude (area under autocorrelation peak) across 4 datasets for raw data and sinusoidal fit. Colour shows phase-shift associated with max/min for individual datasets. Right: Average modulation of burst magnitude averaged across datasets. h Same but for LFP power at seizure frequency. Error bars indicate s.e.m. over datasets. R and P values from circular linear correlation over datasets.

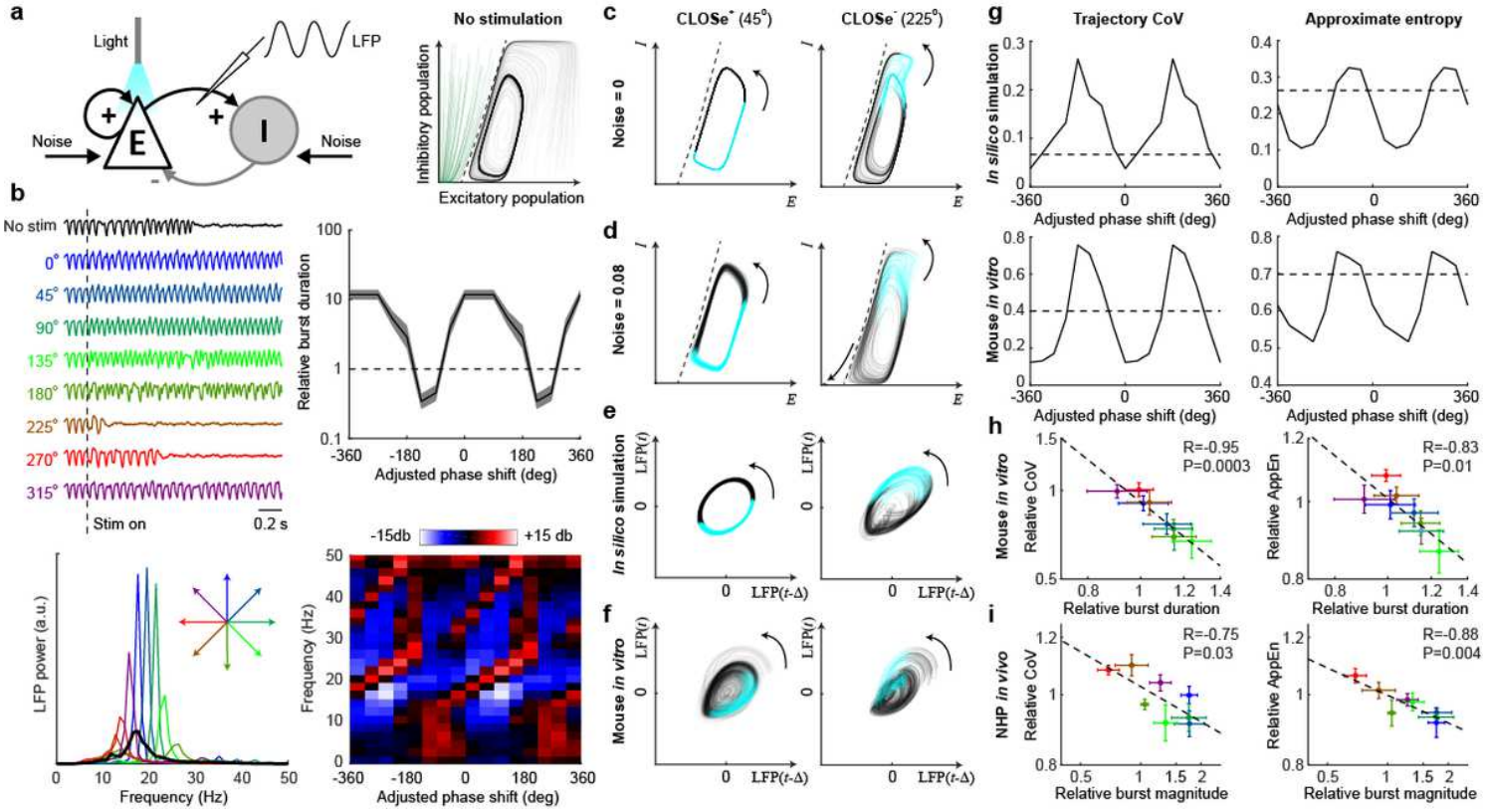

Figure 5

In silico model suggests CLOSe can stabilise/destabilise seizure cycles. a Left: Schematic of in silico model comprising interconnected excitatory (E) and inhibitory (I) populations with white noise input. Right: Model trajectories evolving in the state-space. In the absence of noise, trajectories in green converge on a stable fixed point while trajectories in grey converge on a limit cycle. Dashed line indicates the separatrix between these regions. b Top left: Simulated seizure bursts under CLOSe with different phase-shifts. Simulations were initiated on the limit cycle prior to onset of CLOSe (dashed line), and used the same noise input. Top right: Modulation of burst duration relative to no stimulation for different

CLOSe phase-shifts. Shading indicates s.e.m. over 20 iterations with different noise seeds. Bottom: Modulation of LFP power relative to no stimulation. c State-space trajectories under CLOSe+ and CLOSe- in the absence of noise. Blue indicates when stimulation is delivered. Note that CLOSe- increases the complexity of the trajectory. See Supp. Movie 1 for trajectories under all phase-shifts. d State-space trajectories in the presence of noise. The trajectory fluctuations under CLOSe- are exacerbated, increasing the probability that noise takes the system into the point attractor basin. e Model dynamics reconstructed from delay-embedding of simulated LFP. Under CLOSe+ the LFP traces consistent cycles, while under CLOSe- the trajectory is more complex and variable. f Delay-embedded trajectories for example in vitro session show a similar pattern. g Cycles were quantified with trajectory coefficient of variation (CoV, left) and approximate entropy (AppEn, right). Both are modulated by CLOSe phase-shift relative to no stimulation (dashed line) for in silico (top) and in vitro (bottom) data. h CoV (left) and AppEn (right) plotted against burst modulation for different CLOSe phase-shifts, averaged across all 10 mouse in vitro sessions. i Same but for the 4 NHP in vivo datasets. R and P values from linear correlation across phase-shifts.

Supplementary Files

This is a list of supplementary files associated with this preprint. Click to download.

- suppmovie1.avi